The dichotomy in noble gas signatures linked to tectonic deformation in Wufeng-Longmaxi Shale, Sichuan Basin

Rui Liu [a], Tao Wen [b,*], Julien Amalberti [c], Jian Zheng [d], Fang Hao [e], Dingchuan Jiang [a]

[a] School of Geoscience and Technology, Southwest Petroleum University, Chengdu 610500, PR China
[b] Department of Earth and Environmental Sciences, Syracuse University, Syracuse, New York 13244, United States
[c] Institut für Geowissenschaften, Universität Potsdam, 14476 Potsdam, Germany
[d] Sichuan Changning Natural Gas Development LLC, Chengdu 610051, PR China
[e] School of Geosciences, China University of Petroleum, Qingdao 266580, PR China

ABSTRACT

Geochemical homogeneity in shale is often assumed when tracing subsurface fluids and characterizing sedimentary basins. This study presents measurements of the bulk gas composition, stable isotopes, and noble gas volume fraction and isotopes for shale gas samples collected from gas wells in the Wufeng-Longmaxi Shale, the southern Sichuan Basin, China. The dryness $[C_1/(C_2 + C_3)]$ ranging from 166.3 to 251.2, combined with $\delta^{13}C_1$ and δDC_1 that vary from −28.8 to −27.3‰ and − 153 to −145‰, respectively, point to a late mature thermogenic origin of hydrocarbon gas. $^3He/^4He$ ratios of gas samples are around 0.01 times the air value suggesting dominantly crust-derived He. $^{21}Ne/^{22}Ne$ and $^{40}Ar/^{36}Ar$ ratios of many gas samples are higher than the corresponding air values indicating the mixing of crustal and atmospheric noble gases. Multiple dichotomous patterns are observed in noble gas signatures of forelimb and backlimb samples, and depression and crest samples. $^{20}Ne/^{22}Ne$ ratios of some crest samples are higher than that of depression samples in the backlimb, pointing to the presence of diffusion-driven fractionation that is likely caused by the long-distance migration from depression to crest. Elemental ratios of air-derived noble gas isotopes – $^{22}Ne/^{36}Ar$, $^{84}Kr/^{36}Ar$, and $^{132}Xe/^{36}Ar$ are compared to the recharge water values, suggesting the interactions of oil, gas, and water phases in the shale over geologic time. Forelimb samples generally display older ages than backlimb samples, indicating a larger flux of external radiogenic ^4He due to the higher density of deep faults in the forelimb area caused by the basement-involved deformation. The basement-involved deformation also causes pore collapse especially in the forelimb leading to a lower porosity that results in a more pristine noble gas signature in the forelimb due to the reduced impact of younger recharge water.

1. Introduction

The recent extensive drilling of a large number of gas wells tapping into the deep shale formation with low permeability provides a valuable opportunity to collect crustal fluids that are previously inaccessible, which renders it possible to conduct geochemical characterization of the basin (Hao and Zou, 2013; Milkov et al., 2020), and the assessment of transport and interaction of crustal fluids (e.g., water, gas, and oil) in the basin (Battani et al., 2000; Darrah et al., 2015; Larter et al., 1996; Li et al., 2020; Wen et al., 2017). In previous studies, it is not uncommon to assume that the shale is geochemically homogeneous, although geochemical proxies might vary significantly within the low permeability shale over tens to hundreds of kilometers as pointed out by some

recent work (Byrne et al., 2018, 2020; Györe et al., 2021; Wen et al., 2016).

Geochemical heterogeneity in the petroleum system, also named as reservoir compartmentalization, describes the segregation of a petroleum accumulation into several individual fluid compartments, across which fluid flow and mass exchange (e.g., hydrocarbon fluids) is largely limited (Smalley and Muggeridge, 2010). The assessment of reservoir compartmentalization is critical because 1) it provides invaluable information for geological and geochemical modeling (e.g., Nguyen et al., 2017), and 2) it also sheds light on the tectonic and thermal history of the corresponding basin (e.g., English et al., 2016). However, the reservoir compartmentalization in the unconventional shale has been poorly studied due to the lack of tools to illustrate the relatively inactive

fluid flow in the low permeability shale.

Noble gases (i.e., He, Ne, Ar, Kr, Xe) have been widely used to characterize the transport and interaction of crustal fluids in sedimentary basins (Ballentine et al., 2002; Barry et al., 2016; Byrne et al., 2018; Cao et al., 2018; Darrah et al., 2014; Hunt et al., 2012; Wen et al., 2015, 2016, 2017, 2018). Unlike other geochemical proxies (e.g., stable carbon isotopes) that can be altered by thermochemical reaction, microbial activity, and/or oxidation (Ballentine et al., 1991; Ozima and Podosek, 2002; Porcelli et al., 2002), the modifications of noble gases signatures are solely controlled by physical mechanisms such as dissolution, mixing, advection, and diffusion (Ballentine et al., 2002), which has made noble gas a powerful tool for tracing subsurface fluids including natural hydrocarbon and artificially sequestrated CO_2 since the 1960s (e.g., Ballentine et al., 1991; Barry et al., 2016; Battani et al., 2000; Györe et al., 2015; Li et al., 2020; Pinti and Marty, 1995; Prinzhofer et al., 2010; Schlegel et al., 2011; Zartman et al., 1961). For example, noble gas signatures of natural gas samples collected from the shales in the Americas were recently used to 1) determine the mechanism and timing of hydrocarbon generation (Györe et al., 2021; Schlegel et al., 2011;

Wen et al., 2015); 2) monitor the suspected fugitive gases from shale gas production (Darrah et al., 2014, 2015; Hunt et al., 2012; Wen et al., 2015, 2016, 2017); 3) constrain the efficiency of gas expulsion or retention (Byrne et al., 2018, 2020; Hunt et al., 2012); and 4) determine the timing of CO_2 emplacement into shale (Györe et al., 2021). The lack of consideration of reservoir compartmentalization in these previous studies might have largely hampered the advancements of characterization of relevant geological processes. For example, the observed lateral variability in noble gas signatures within the Antrim Shale in the Michigan Basin (Wen et al., 2015) and within the Eagle Ford shale in southern Texas (Byrne et al., 2018), respectively, might have important implications for the reservoir compartmentalization within the low permeability shale.

In this study, we present noble gas and stable carbon isotopic analyses of shale gas samples collected from gas wells in the Wufeng-Longmaxi Shale located within the southern Sichuan Basin in China (Fig. 1). As the most prolific shale play, the Wufeng-Longmaxi Shale contains the largest technically recoverable shale gas resources in China. However, it has been poorly studied for its reservoir
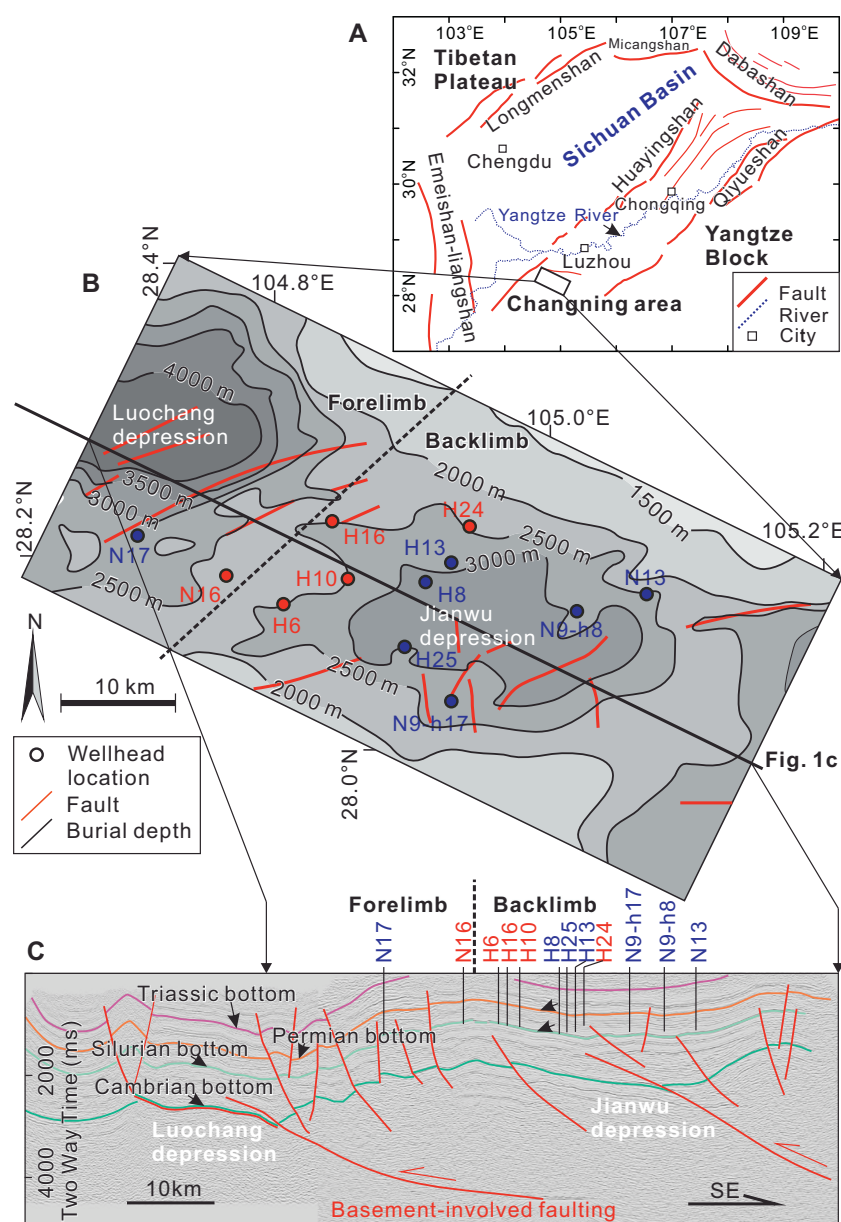
Fig. 1. (A) Map showing the geographic distribution of the Changning area in the Sichuan Basin, China. (B) The burial depth contours of the top of the Wufeng-Longmaxi Shale. Wellhead locations are shown as black circles, which are filled by blue and red for anticline depression and crest locations, respectively. (C) The seismic reflection profile in the Changning area, showing a basement-involved thrust folding that can be divided into forelimb and backlimb areas. (For interpretation of the references to colour in this figure legend, the reader is referred to the web version of this article.)

compartmentalization as well as the associated fluid interactions. This work is the first to assess the reservoir compartmentalization in the Wufeng-Longmaxi Shale as well as to discover the underlying geologic mechanisms including tectonic activities and interactions of subsurface fluids. In this study, we strive to use the Wufeng-Longmaxi Shale as a testbed to explore the interplays of reservoir compartmentalization, tectonic deformation, and the multi-phase interaction of oil, water, and gas.

2. Geological setting

The Sichuan Basin is located in southwest China (approximately 28°N to 33°N, 102°E to 110°E) showing a sizeable (>1.8 × 10^4 km^2) rhomboid shape that is bounded by thrust-fold belts on all sides (Liu et al., 2019, 2020a, 2020b) (Fig. 1). The basin, located in the western Yangtze Block, has experienced a transformation from the passive margin to the foreland basin during the Middle Mesozoic (Meng et al., 2005; Wang et al., 2013; Yan et al., 2003). Sediments of the Sichuan Basin are up to 12 km thick consisting of multiple prolific petroleum systems (Fig. S1).

The Wufeng-Longmaxi Shale, mainly of black carbonaceous shale, was deposited in the deep-water shelf of the Yangtze Block during the Late Ordovician and Early Silurian (i.e., 445 to 440 Ma). Because of the high total organic carbon (TOC) content (up to 6–8 wt%) (Liu et al., 2020a, 2020b), the Wufeng-Longmaxi Shale is one of the primary source rocks in the Sichuan Basin (Fig. S1).

The Wufeng-Longmaxi Shale that underlies the Changning area of the southern Sichuan Basin has been targeted for unconventional shale gas production since 2012, and it is now one of the most prolifically produced shale gas fields in China (China National Petroleum Corporation, 2020) (Fig. 1b). Industrial drillings in the Changning area reveal that the Wufeng-Longmaxi Shale has a present burial depth ranging from 2000 m on anticline crest to 4000 m in syncline depression and a present geothermal gradient of 23 °C/km (Fig. 1). Solid bitumen reflectance and basin modeling indicate that the thermal maturity of the Wufeng-Longmaxi Shale is a 2.5–3% vitrinite reflectance equivalent, suggesting a maximum burial depth of approximately 6 km (Dai et al., 2014; Hao et al., 2013). Seismic reflection shows that the Wufeng-Longmaxi Shale was exhumed and deformed by a basement-involved thrust folding (Fig. 1) (Liu et al., 2020b). During the basement-involved folding, the deformation in the forelimb is more extreme than in the backlimb (Scanlin and Engelder, 2003) (Fig. 1). Relative to an average porosity of approximately 6% in the Wufeng-Longmaxi Shale, the average shale porosity in the forelimb was reduced to approximately 4% by the pore collapse during the tectonic deformation (Liu et al., 2020b).

3. Samping and analytical methodology

A total of 24 gas samples (2 samples per well) were collected from 12 production wells that tap into the Wufeng-Longmaxi Shale in the Changning area in June 2019 (Fig. 1B). Based on the structural position, sampled gas wells are clustered into crest and depression groups (Table 1). Among these 12 gas wells, two wells (i.e., N17 and N16) are located in the forelimb underlain by the basement-involved anticline while 10 wells are drilled in the area of anticline backlimb.

Natural gases were sampled directly from the wellhead (the valve on the wellhead was opened to control the well pressure at 20–60 bar) using a manifold to reduce the gas pressure before flowing the gas into the aluminum IsoTube® gas containers (IsoTech Laboratories, Champaign IL, USA) at 2–3 bar. Air contamination during sampling was minimized by allowing the gas to flush through the system for approximately 10 min before shutting off the valve that connects IsoTube® and the wellhead.

For each well, one IsoTube® sample was sent to the IsoTech Laboratories for the analyses of major gas composition (i.e., C$_1$, C$_2$, C$_3$, N$_2$, O$_2$, CO$_2$) using Shimadzu 2010 Gas Chromatograph and carbon (δ^{13}C) and analyses of hydrocarbon (δD) isotope of methane (C$_1$) and ethane (C$_2$) using HP6890 GC interfaced to Thermo Scientific® Delta V Plus (Table 1). δ^{13}C and δD values are presented relative to the PDB and SMOW standards, respectively.

The other set of IsoTube® samples were shipped to and analyzed in the Noble Gas Laboratory at the University of Michigan for the complete suite of stable noble gases (He, Ne, Ar, Kr, Xe) within approximately two weeks of sample collection (Tables 2 and 3). Collected gas samples were transferred from IsoTube® to the copper tube, which then were attached to a vacuum extraction and purification system. Following the extraction and purification, He and Ne were analyzed in a Thermo Scientific® Helix SFT mass spectrometer while Ar, Kr, and Xe were sequentially inlet into a Thermo Scientific® ARGUS VI mass spectrometer using a Janis computer-controlled double-head cryo-separator. Detailed steps of extraction, purification, and analysis procedures were described in the literature (Wen et al., 2017). Standard errors for volume fractions are 1.5, 1.3, 1.3, 1.5, and 2.2% for He, Ne, Ar, Kr, and Xe, respectively (Table 3).

In addition, the depth profile of U, Th, and K concentrations in the rock from both forelimb and backlimb areas are derived from in-hole spectral gamma borehole logging provided by the Sichuan Changning Natural Gas Development LLC (Fig. S2).

Table 1
Major gas species and stable (carbon and hydrogen) isotopes of shale gas samples were collected from the Wufeng-Longmaxi Shale in the Changning area[a].

Well	Well depth (m)	Structural location		Major gas composition (vol%)						C$_1$/(C$_2$ + C$_3$)	(‰VPDB)		(‰VSMOW)
				C$_1$	C$_2$	C$_3$	O$_2$	CO$_2$	N$_2$		δ^{13}C$_1$	δ^{13}C$_2$	δDC$_1$
N16	2345	Crest	Forelimb	98.85	0.42	0.01	0.04	0.30	0.36	232.6	−28.1	−33.6	−147
H10	2503	Crest	Backlimb	98.74	0.52	0.01	0.04	0.36	0.31	186.4	−28.0	−33.9	−145
H16	2535	Crest	Backlimb	98.82	0.44	0.01	0.05	0.34	0.32	221.3	−28.8	−34.4	−146
H24	2573	Crest	Backlimb	98.74	0.45	0.01	0.07	0.34	0.37	214.9	−28.6	−34.1	−146
H6	2682	Crest	Backlimb	98.69	0.39	0.01	0.08	0.44	0.36	251.2	−27.8	−34.1	−149
N17	3067	Depression	Forelimb	0.09	0.00	0.00	20.96	0.05	78.00	nd[b]	nd	nd	nd
H13	3040	Depression	Backlimb	98.83	0.43	0.01	0.02	0.41	0.28	224.1	−28.5	−34.3	−153
N9-h17	3088	Depression	Backlimb	98.60	0.58	0.02	0.06	0.38	0.35	166.3	−27.4	−33.6	−150
N9-h8	3103	Depression	Backlimb	98.72	0.43	0.01	0.04	0.41	0.37	226.1	−27.6	−32.9	−148
H25	3132	Depression	Backlimb	98.73	0.54	0.02	0.05	0.33	0.32	177.8	−27.4	−32.8	−148
N13	3140	Depression	Backlimb	98.84	0.48	0.01	0.03	0.27	0.35	202.4	−27.8	−33.5	−148
H8	3250	Depression	Backlimb	98.42	0.45	0.01	nd	0.38	0.41	212.6	−27.3	−32.9	−152

[a] Errors are ±0.1% for concentrations and ± 0.1‰ for isotope ratios.
[b] "nd" denotes no data.

Table 2

Noble gas isotope ratios of shale gas samples collected from the Wufeng-Longmaxi Shale in the Changning area[a].

Well	^{3}He/^{4}He[b]	^{20}Ne/^{22}Ne	^{21}Ne/^{22}Ne	^{38}Ar/^{36}Ar	^{40}Ar/^{36}Ar	^{86}Kr/^{84}Kr	^{136}Xe/^{130}Xe
N16	0.0102(4)	9.59(9)	0.0351(13)	0.1991(44)	1071(4)	0.3089(9)	2.157(24)
H10	0.0105(5)	9.72(12)	0.0248(37)	0.2125(77)	540(4)	0.3040(17)	2.084(59)
H16	0.0100(4)	9.90(4)	0.0315(5)	0.1928(17)	590 (1)	0.3068(6)	2.183(12)
H24	0.0104(4)	9.95(2)	0.0304(2)	0.1898(12)	458 (1)	0.3080(5)	2.172(10)
H6	0.0096(2)	9.97(2)	0.0296(4)	0.1888(8)	455(1)	0.3074(4)	2.166(8)
N17	0.0103(3)	9.67(5)	0.0418(8)	0.1935(27)	1360(2)	0.3096(8)	2.178(14)
H13	0.0106(3)	9.76(8)	0.0344(10)	0.1948(31)	864(3)	0.3069(9)	2.161(19)
N9-h17	0.0095(3)	9.90(3)	0.0322(5)	0.1883(14)	628(1)	0.3079(7)	2.164(14)
N9-h8	0.0094(3)	9.86(4)	0.0332(7)	0.1914(25)	710(2)	0.3069(10)	2.193(16)
H25	0.0093(4)	9.80(6)	0.0325(6)	0.1948(29)	751(1.8)	0.3072(13)	2.183(17)
N13	0.0102(4)	9.81(5)	0.0338(9)	0.1922(32)	733(1.7)	0.3085(7)	2.184(20)
H8	0.0093(2)	9.85(4)	0.0329(5)	0.1921(12)	690(1)	0.3062(9)	2.183(12)
Air[c]	1	9.80(8)	0.0290(2)	0.1885(3)	298.6(3)	0.3052(25)	2.176(3)

[a] 1σ standard deviation is shown as the last significant figures in parentheses.

[b] ^{3}He/^{4}He ratio is reported in units of R_A, where R_A is the air ratio of $(1.384 \pm 0.013) \times 10^{-6}$ (Clarke et al., 1976; Mishima et al., 2018; Ozima and Podosek, 2002).

[c] Air values of ^{3}He/^{4}He, ^{20}Ne/^{22}Ne, ^{21}Ne/^{20}Ne, ^{40}Ar/^{36}Ar were derived from Clarke et al. (1976), Eberhardt et al. (1965), and Györe et al. (2019), respectively. Other air values are derived from Ozima and Podosek (2002).

Table 3

Noble gas isotopic concentrations of shale gas samples collected from the Wufeng-Longmaxi Shale in the Changning area[a].

Well	^{4}He($\times 10^{-4}$)	^{20}Ne($\times 10^{-8}$)	^{36}Ar($\times 10^{-8}$)	^{84}Kr($\times 10^{-10}$)	^{132}Xe($\times 10^{-11}$)	^{4}He$_{rad}$($\times 10^{-4}$)	^{40}Ar$_{rad}$($\times 10^{-5}$)	^{4}He$_{rad}$/^{40}Ar$_{rad}$	(^{40}Ar/^{36}Ar)$_{predicted}$[d]
N16	1.80(3)	0.82(1)	3.16(4)	9.0(1)	6.6(2)	1.80(3)	2.44(3)	7.37	524.5
H10	1.95(3)	2.36(3)	6.32(8)	17.5(5)	10.6(2)	1.95(3)	1.53(3)	12.78	420.9
H16	1.86(3)	2.48(3)	6.87(9)	13.3(2)	10.9(3)	1.86(3)	2.02(3)	9.29	406.0
H24	1.54(2)	4.77(6)	11.19(15)	22.9(3)	18.0(4)	1.54(2)	1.78(2)	8.63	353.2
H6	1.89(3)	5.85(8)	13.71(18)	29.4(4)	23.0(5)	1.89(3)	2.14(3)	8.81	353.2
N17	5.07(8)	1.89(2)	6.66(9)	12.1(2)	9.6(2)	5.07(8)	7.07(9)	7.17	600.5
H13	1.64(2)	1.01(1)	3.49(5)	8.2(1)	7.1(2)	1.64(2)	1.97(2)	8.31	485.0
N9-h17	2.01(3)	2.31(3)	6.14(8)	12.9(2)	10.6(2)	2.01(3)	2.02(3)	9.94	428.4
N9-h8	1.86(3)	1.95(3)	5.72(7)	11.7(2)	9.7(2)	1.86(3)	2.35(3)	7.90	427.5
H25	1.66(3)	1.56(2)	4.71(6)	8.0(1)	7.8(2)	1.66(3)	2.13(3)	7.79	438.4
N13	1.68(3)	1.63(2)	4.85(6)	10.1(2)	8.4(2)	1.68(3)	2.11(3)	7.97	436.0
H8	1.79(3)	1.90(2)	7.22(9)	5.8(1)	10.5(2)	1.80(3)	2.83(4)	6.37	397.5
Air[b]	0.0524(5)	1645(4)	3142(3)	6498(57)	2340(27)	nd[c]	nd	nd	nd

[a] 1σ standard deviation is shown as the last significant figures in parentheses. Units are in cm³STP/cm³ with standard conditions after Ozima and Podosek (2002) (P = 0.101 MPa, T = 0 °C).

[b] Air values were derived from Eberhardt et al. (1965), Györe et al. (2019), Lee et al. (2006), Mark et al. (2011), and Ozima and Podosek (2002).

[c] "nd" denotes no data.

[d] These ^{40}Ar/^{36}Ar values were calculated by assuming all He and Ar gases in the samples were produced in-situ within the Wufeng-Longmaxi Shale as following Eq. 6. More details about the calculation can be found in the Discussion section.
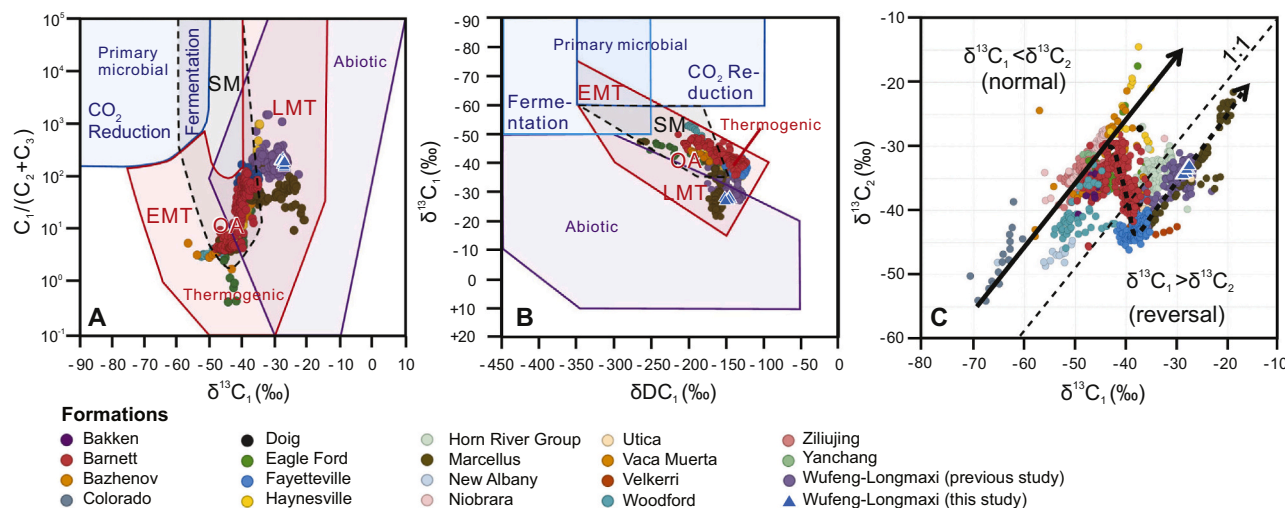
Fig. 2. Gas molecular and stable isotopic composition plots of the Wufeng-Longmaxi Shale (Changning area) along with other shales. $C_1/(C_2 + C_3)$ vs. $\delta^{13}C_1$ (A) and $\delta^{13}C_1$ vs. δDC_1 (B) of well gases are consistent with gases of thermogenic origin. (C) The isotopic composition of ethane exhibit a reversal trend of increasing maturity. Gas genetic diagrams were adapted from Milkov et al., (2020). Data of other shales were compiled by Milkov et al., (2020). Abbreviations: SM – secondary microbial, EMT – early mature thermogenic gas, OA – oil-associated (mid-mature) thermogenic gas, LMT – late mature thermogenic gas.

4. Results

4.1. Major gas composition, carbon stable isotopes, and rock chemistry

Sample ID, well depth, major gas species composition, and stable isotopes for 12 gas samples from 12 wells within the Wufeng-Longmaxi Shale are shown in Table 1. One sample from well N17 was likely contaminated by air after sampling with 78.00 vol% of N_2 and 20.96 vol % O_2, although noble gas signatures of its replicate were well preserved (section 4.2). The other 11 well-preserved gas samples consist of methane (C_1) ranging from 98.42 to 98.85 vol%, heavier hydrocarbons ethane (C_2) and propane (C_3) contributing a total of less than 0.6 vol%, CO_2 (0.3 to 0.44 vol%), and N_2 (0.28 to 0.41 vol%). The gas dryness [i.e., $C_1/(C_2 + C_3)$ ratio] of these samples is high, ranging from 166.3 to 251.2, which indicates that the hydrocarbon might be of late mature thermogenic origin (Milkov et al., 2020) (Fig. 2A). This hydrocarbon origin is consistent with the high thermal maturity level derived from the solid bitumen reflectance study (Dai et al., 2014; Hao et al., 2013).

Stable carbon isotopic ratios of $\delta^{13}C_1$ and $\delta^{13}C_2$ range from −28.8 to −27.3‰ and − 34.4 to −32.8‰, respectively (Fig. 2). Stable hydrogen isotopic ratio of methane (δDC_1) ranges from −153 to −145‰ (Fig. 2B). Both $\delta^{13}C_1$ and δDC_1 values of our samples also argue a late mature thermogenic origin of hydrocarbon (Milkov et al., 2020).

U, Th, and K contents in the solid phase in both forelimb and backlimb are plotted against the depth in Fig. S2. Forelimb and backlimb drilling cores present similar rock chemical compositions regarding these three elements.

4.2. Noble gas signatures

The results of He, Ne, Ar, Kr, and Xe concentrations and isotopic ratios of 12 Wufeng-Longmaxi gas samples are listed in Tables 2 and 3. The corresponding air values (Clarke et al., 1976; Eberhardt et al., 1965; Györe et al., 2019; Mark et al., 2011; Ozima and Podosek, 2002) are also reported in the table for reference.

^4He concentrations of gas samples in this study range from (1.54 ± 0.02) to (5.07 ± 0.08) × 10^{-4} cm^3STP/cm^3. $^3He/^4He$ values range from (0.0093 ± 0.0004)R_A to (0.0106 ± 0.0003)R_A (Figs. 3, 4A), where R_A is the air ratio of (1.384 ± 0.013) × 10^{-6} (Clarke et al., 1976; Mishima

et al., 2018; Ozima and Podosek, 2002).

$^{20}Ne/^{22}Ne$ and $^{21}Ne/^{22}Ne$ ratios of the samples vary from 9.59 ± 0.09 to 9.97 ± 0.02 and from 0.0248 ± 0.0037 to 0.0418 ± 0.0008, respectively (Table 2; Fig. 4B, C). Most of $^{21}Ne/^{22}Ne$ ratios are higher than the air value of 0.02959 (Eberhardt et al., 1965; Györe et al., 2019) (Fig. 4C), indicating a mixing of two endmembers: crustal and atmospheric Ne. Both $^{21}Ne/^{22}Ne$ and $^{20}Ne/^{22}Ne$ ratios display a dichotomy between forelimb and backlimb samples with higher $^{21}Ne/^{22}Ne$ but lower $^{20}Ne/^{22}Ne$ ratios in the forelimb samples.

$^{40}Ar/^{36}Ar$ ratios of the samples vary from 455 ± 1 to 1360 ± 2, much higher than the air value of 298.56 (Mark et al., 2011) (Fig. 4D). These high $^{40}Ar/^{36}Ar$ ratios point to a major contribution of radiogenic ^{40}Ar (denoted as $^{40}Ar_{rad}$). Similar to $^{21}Ne/^{22}Ne$ ratios, a dichotomy pattern is also observed in $^{40}Ar/^{36}Ar$ ratios between forelimb and backlimb samples: forelimb samples report $^{40}Ar/^{36}Ar$ ratios larger than 1000, while $^{40}Ar/^{36}Ar$ ratios of backlimb samples are from 400 to 900 (Fig. 4D). All the samples show a very low level of Ar volume fraction that is generally <1% of Ar content in the air [i.e., (934 ± 1) × 10^{-5} cm^3STP/cm^3; Lee et al., 2006; Ozima and Podosek, 2002], which supports that all gas samples are very well preserved (i.e., lack of air contamination).

The majority of samples display $^{86}Kr/^{84}Kr$ ratios similar to or slightly higher than the air value of 0.3052 (Ozima and Podosek, 2002) (Fig. 4E). All the samples report $^{136}Xe/^{130}Xe$ values that are indistinguishable from the air value of 2.176 (Ozima and Podosek, 2002) (Fig. 4F), pointing to the absence of a significant contribution of terrigenic Xe.

5. Discussion

5.1. Spatial variability in crustal noble gases

Noble gases in most subsurface fluids from sedimentary systems are dominated by an atmospheric origin (e.g., ^{22}Ne, ^{36}Ar, ^{84}Kr, ^{132}Xe) and/ or a crustal component (e.g., ^4He, ^{21}Ne, and ^{40}Ar) derived primarily from the nuclear reaction of their parent elements (Ballentine and Burnard, 2002; Ozima and Podosek, 2002), while mantle-contributed noble gases are sometimes identified in crustal fluids in sedimentary basins (Gilfillan et al., 2008, 2019; Györe et al., 2018; Karolytė et al., 2019; Ma et al., 2009). Radiogenic or nucleogenic noble gases ^4He, ^{21}Ne, and ^{40}Ar are denoted as $^4He_{rad}$, $^{21}Ne_{nuc}$, and $^{40}Ar_{rad}$, although these
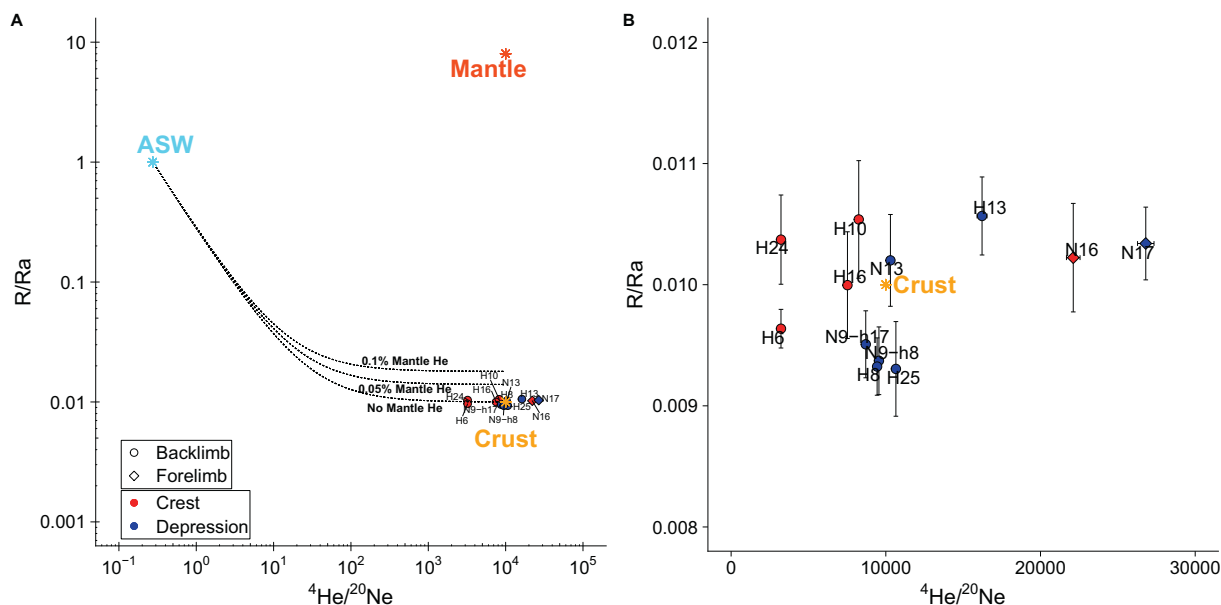

Fig. 3. (A) $^3He/^4He$ versus $^4He/^{20}Ne$ ratios for all gas samples in this study. The mixing lines representing the mixing of air- and crust-derived noble gases, and air- and mantle-derived noble gases are also shown. $^3He/^4He$ and $^4He/^{20}Ne$ ratios of air, crust, and mantle endmembers are 1 and 0.274 (Ozima and Podosek, 2002), 0.01 and 10,000, 8 and 10,000 (Ballentine and Burnard, 2002; Graham, 2002; Oxburgh et al., 1986), respectively. (B) a zoom-in view of the sample cluster in (A).
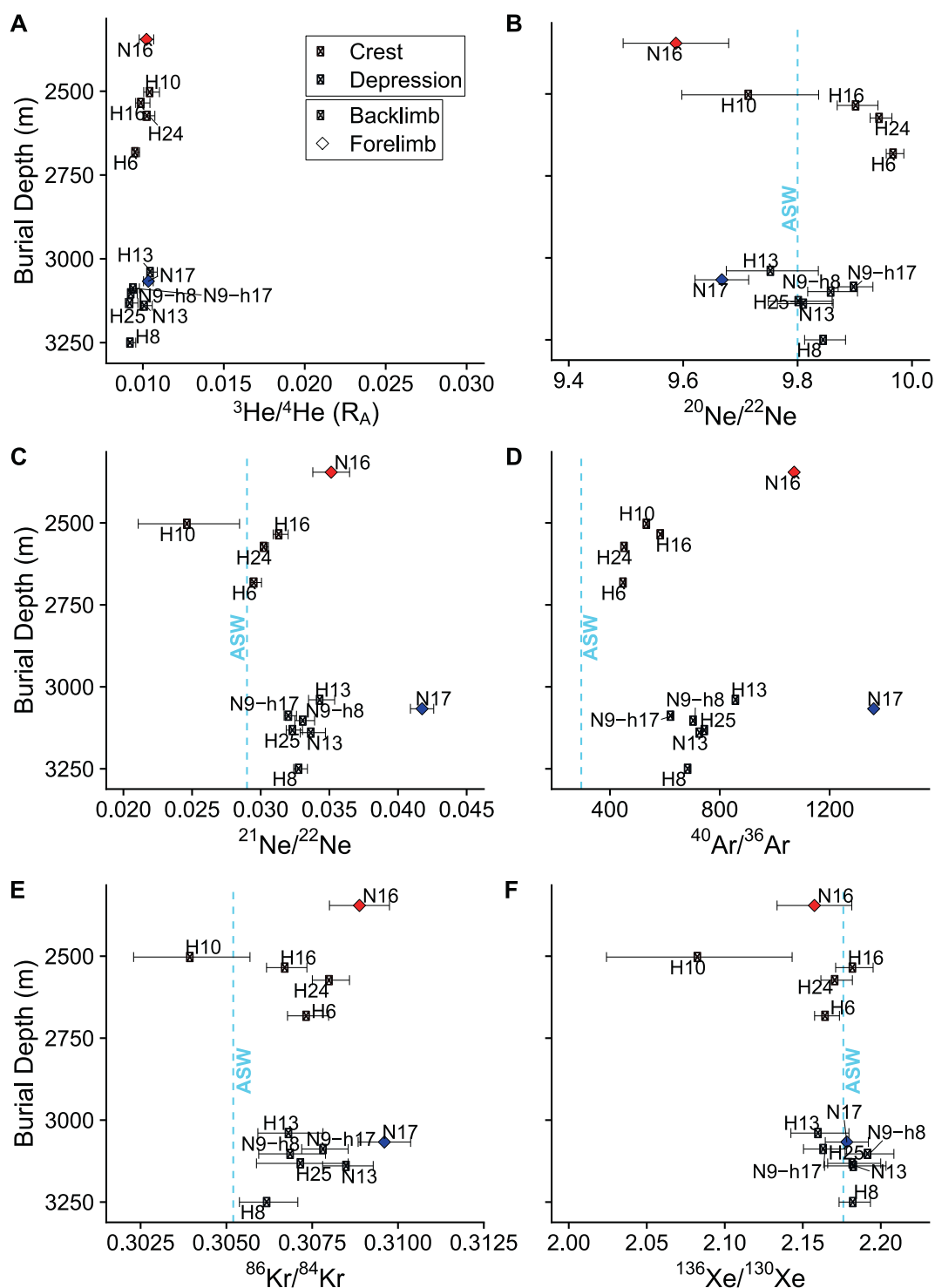
Fig. 4. Depth profiles of (A) ^{3}He/^{4}He, (B) ^{20}Ne/^{22}Ne, (C) ^{21}Ne/^{22}Ne, (D) ^{40}Ar/^{36}Ar, (E) ^{86}Kr/^{84}Kr, and (F) ^{136}Xe/^{130}Xe ratios. Crest samples are much shallower than depression samples. The contribution of crustal noble gases is likely the largest in the forelimb sample N17 compared to other samples, particularly those collected from backlimb area. Corresponding ASW values are indicated (Ozima and Podosek, 2002).

isotopes can also be of atmospheric origin.

5.1.1. Crustal helium

The typical ^{3}He/^{4}He values of crust and mantle noble gases are ~0.01R_A and 8R_A, respectively, while both sources report ^{4}He/^{20}Ne ratios as high as 10,000 (Ballentine and Burnard, 2002; Graham, 2002; Oxburgh et al., 1986). In contrast, ^{4}He/^{20}Ne ratio of atmosphere-derived noble gases (i.e., ASW) is 0.274 by assuming the recharge water is seawater with a salinity of 0.6 M in equilibrium with atmosphere at 25 °C (i.e., the initial deposition environment of the Wufeng-Longmaxi Shale) (Ozima and Podosek, 2002). The mixing patterns of atmosphere-, crust-, and mantle-derived noble gases are presented in Fig. 3, which clearly indicate that, He in all the samples are dominated by crustal He (i.e., > 99.95%). Nevertheless, forelimb wells, N16 and N17, present the highest ^{4}He/^{20}Ne among all sampled gases indicating a higher amount of crustal noble gases than that of backlimb wells.

Crustal $^4He_{rad}$ is produced by the radioactive decay of U and Th in host rocks. By assuming that measured ^4He in the collected Wufeng-Longmaxi gas samples is a mixing of two endmembers: atmosphere and crust, we can calculate the contribution of $^4He_{rad}$ as follows (Ballentine et al., 2002) (Table 3):

$$^4He_{rad} = \,^4He_{measured} \times \frac{R_A - R_{measured}}{R_A - R_c} \qquad (1)$$

where the subscript of *measured* denotes the measured noble gas ratio. R_c is assumed to be $0.01R_A$, i.e., 1.384×10^{-8} (Ballentine and Burnard, 2002). $^4He_{rad}$ contents of our gas samples calculated by Eq. 1 account for 99.94%–100% of the total measured ^4He (Table 3), which is consistent with the observation from Fig. 3.

5.1.2. Crustal argon and neon

Crustal $^{40}Ar_{rad}$ in the subsurface fluids is produced by the radioactive decay of ^{40}K in the crustal host rock (Ballentine and Burnard, 2002). By assuming a mixing of atmospheric and radiogenic Ar in the Wufeng-Longmaxi Shale, the $^{40}Ar_{rad}$ contents can be calculated as follows (Ballentine et al., 1991):

$$^{40}Ar_{rad} = \,^{40}Ar_{measured} \times \left[1 - \left(\frac{^{40}Ar}{^{36}Ar}\right)_{air} \middle/ \left(\frac{^{40}Ar}{^{36}Ar}\right)_{measured} \right] \qquad (2)$$

where $(^{40}Ar/^{36}Ar)_{air} = 298.56$ (Lee et al., 2006; Mark et al., 2011). $^{40}Ar_{rad}$ values calculated by Eq. 2 are listed in Table 3, which account for 34%–78% of the total ^{40}Ar concentration with the contribution of atmospheric Ar varying from 22%–66%.

The highest contribution of $^{40}Ar_{rad}$ was found in two forelimb wells N16 (72%) and N17 (78%). Below, we explore the potential cause of the higher contribution of $^{40}Ar_{rad}$ in forelimb wells for two scenarios: 1) the Wufeng-Longmaxi Shale is a closed-system where $^{40}Ar_{rad}$ is produced only in-situ within the shale, although the production rate of $^{40}Ar_{rad}$ could vary by location; 2) the Wufeng-Longmaxi Shale is an open system, and forelimb and backlimb wells might have a different amount of exchange (loss or gain) of Ar with external formations. The spectral gamma ray logs of the Wufeng-Longmaxi Shale in the Changning area show the similarity of concentrations of parent radionuclide concentrations (i.e., U, Th, K) in the solid phase (Fig. S2) between forelimb and backlimb; thus, it is likely that the $^{40}Ar_{rad}$ production rate in the host rocks of both forelimb and backlimb areas might be similar. Therefore,

the first scenario – Wufeng-Longmaxi Shale is a closed system – is unlikely to account for the observed variability in $^{40}Ar_{rad}$ between forelimb and backlimb.

Fig. 5A shows $^{40}Ar/^{36}Ar$ ratio versus $1/^{36}Ar$ for all gas samples in this study. The corresponding air value is also indicated in the figure. Higher $^{40}Ar/^{36}Ar$ and $1/^{36}Ar$ values in the plot point to a larger crustal contribution while lower values indicate a larger atmospheric contribution. Except for well N17, all of the other wells fall on a linear regression line of $^{40}Ar/^{36}Ar = 2.2 \times 10^{-5} \times 1/^{36}Ar + 298.56$, which points to the mixing of two endmembers: air- and crust-derived. The volume fraction of $^{40}Ar_{rad}$ in the crustal endmember is defined by the slope of the regression line, e.g., 2.2×10^{-5} for all Wufeng-Longmaxi wells except for N17. The observation that well N16 is located slightly above the regression line likely reflecting a slightly higher $^{40}Ar_{rad}$ content for N16 than that of backlimb wells. For well N17, the slope of the regression line is up to 7.1×10^{-5}, implying a mixing of atmospheric Ar and a crustal endmember containing more radiogenic Ar. This likely argues against that the Wufeng-Longmaxi Shale is a closed system with the same $^{40}Ar_{rad}$ endmember for both forelimb and backlimb samples.

A similar conclusion can be drawn by analyzing $^{21}Ne/^{22}Ne$ and $1/^{22}Ne$ values of the gas samples. The well N17 requires a crustal endmember with the volume fraction of $^{21}Ne_{nuc}$ of 2.5×10^{-11} that is higher than that of 5.5×10^{-12} for other wells, whereas well N16 requires a crustal Ne endmember with $^{21}Ne_{nuc}$ content lower than that of N17 but still slightly higher than that of other wells (Fig. 5B).

5.1.3. External sources of crustal helium and argon

The in-situ production rate of $^4He_{rad}$ and $^{40}Ar_{rad}$ within the Wufeng-Longmaxi Shale can be estimated as follows (Ballentine et al., 1991):

$$P\left(^4He\right) = 1.207 \times 10^{-13}[U] + 2.867 \times 10^{-14}[Th] \, cm^3 STP g^{-1}_{rock} yr^{-1} \qquad (3)$$

$$P\left(^{40}Ar\right) = 3.885 \times 10^{-18}[K] \, cm^3 STP g^{-1}_{rock} yr^{-1} \qquad (4)$$

where $[U]$, $[Th]$, and. $[K]$ are the U, Th, and K concentrations (ppm), respectively, which are approximately 15 ppm, 12 ppm, 2.2×10^4 ppm on average as shown in the spectral gamma ray logs of the Wufeng-Longmaxi Shale (Fig. S2). $^4He_{rad}/^{40}Ar_{rad}$ ratio of the in-situ production in the shale can be calculated by:

$$^4He_{rad}/^{40}Ar_{rad} = [3.11 + 0.738([Th]/[U])] \times ([U]/[K]) \times 10^4 \qquad (5)$$
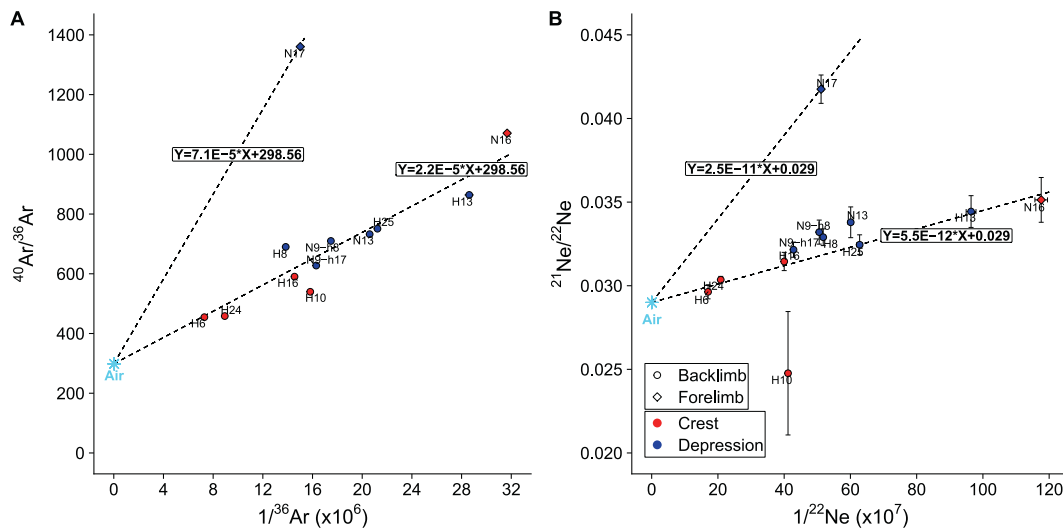
Fig. 5. (A) $^{40}Ar/^{36}Ar$ ratio $1/^{36}Ar$ and (B) $^{21}Ne/^{22}Ne$ ratio $1/^{22}Ne$ for all gas samples. Each regression line represents a mixing of an air endmember and a crust endmember. The slope of the regression lines denotes the content of noble gas in the crust endmember, i.e., ^{40}Ar and ^{21}Ne in panels (A) and (B), respectively. Please refer to the main text for a detailed discussion of this figure. Corresponding air values are indicated and derived from the literature (Eberhardt et al., 1965; Györe et al., 2019; Mark et al., 2011).

Calculated $^4\mathrm{He}_{rad}/^{40}\mathrm{Ar}_{rad}$ of the in-situ production in the Wufeng-Longmaxi Shale is approximately 25.21, much higher than that of all gas samples in this study (Table 3) as well as that of the lower (3.09), middle (5.79), and upper crust (6.0), respectively (Ballentine and Burnard, 2002). However, measured $^4\mathrm{He}_{rad}/^{40}\mathrm{Ar}_{rad}$ ratios of all the samples, ranging from 6.32 to 12.63, are close to deep crust value, which likely suggest the dilution of in-situ produced He and Ar by noble gases sourced from the deep crust.

The closure temperature of radiogenic $^{40}\mathrm{Ar}$ is about 220 °C, only above which produced radiogenic Ar would be released from silicate mineral grains into the subsurface fluids (Hunt et al., 2012). Unlike radiogenic $^{40}\mathrm{Ar}$, radiogenic $^4\mathrm{He}$ can freely exchange between quartz grains and the gas phase at temperatures as low as approximately 25 °C (Hunt et al., 2012; Shuster and Farley, 2005). Differentiated release of Ar and He from rock under low temperatures (i.e., < 220 °C) can lead to elevated $^4\mathrm{He}_{rad}/^{40}\mathrm{Ar}_{rad}$ ratio in the gas phase than that in rock, which is the opposite to what we observe in our gas samples. In addition, a high vitrinite reflectance of 2.6–3.0% (Dai et al., 2014; Hao et al., 2013) indicates a temperature of >220 °C (Gao et al., 2017) at which produced $^{40}\mathrm{Ar}$ from the mineral would be completely released.

Alternatively, episodic loss of noble gas (e.g., $^4\mathrm{He}$) at low temperature can also lower $^4\mathrm{He}_{rad}/^{40}\mathrm{Ar}_{rad}$ (Darrah et al., 2015; Harkness et al., 2017; Moore et al., 2018). Although we cannot completely exclude the possibility of the episodic loss of $^4\mathrm{He}$ at low temperature in the study area, the similarity between calculated $^4\mathrm{He}_{rad}/^{40}\mathrm{Ar}_{rad}$ ratios of collected samples and the deep crust value suggests that the presence of an external source of noble gases with a lower $^4\mathrm{He}_{rad}/^{40}\mathrm{Ar}_{rad}$ ratio in the Wufeng-Longmaxi Shale is very likely and might be more viable.

The $^{40}\mathrm{Ar}/^{36}\mathrm{Ar}$ value associated with the in-situ production can be predicated as:

$$\left(^{40}Ar/^{36}Ar\right)_{predicted} = \left(^{36}Ar_{measured} \times 298.56 + {}^4He/25.21\right)\Big/{}^{36}Ar_{measured} \tag{6}$$

Predicted $^{40}\mathrm{Ar}/^{36}\mathrm{Ar}$ values are listed in Table 3. These predicted values are lower than the measured $^{40}\mathrm{Ar}/^{36}\mathrm{Ar}$ ratios for all gas samples (Tables 2 and 3). This also likely points to an additional source of $^{40}\mathrm{Ar}_{rad}$ from deeper formations in the lower or upper crust external to the Wufeng-Longmaxi Shale.

Measured $^{40}\mathrm{Ar}/^{36}\mathrm{Ar}$ ratios of forelimb wells are higher than that of backlimb wells, which suggests that a higher flux of $^{40}\mathrm{Ar}_{rad}$ from deep crustal fluids might be present in the forelimb area, in particular for well N17. For N17, a higher flux of external crustal fluids is consistent with the observation that N17 is in a locality with a relatively high density of deep faults (Fig. 1B and C), which might facilitate the migration of subsurface fluids from the deeper crust into the Wufeng-Longmaxi Shale. Unlike N17, N16 is located in a region with relatively fewer faults, although N16 still presents a relatively high contribution of crustal Ne and Ar (Figs. 4 and 5). This can be due to either a higher in-situ production rate of radiogenic noble gases in this isolated locality or less contribution of younger recharge water from the surface due to lower porosity in the forelimb area (Liu et al., 2020b).

Within the Changning area, the basement-involved folding over geological time has led to geologic deformation. Such deformation in the forelimb side is more extensive than that in the backlimb area (Liu et al., 2020b), which results in more faults (particularly deep faults) in the forelimb area (Fig. 1) likely facilitating a higher flux of radiogenic He and Ar from the deep crust into the Wufeng-Longmaxi Shale (e.g., N17). In addition, the basement-involved deformation has also led to the decline of bulk porosity due to pore collapse in the forelimb segment of the Wufeng-Longmaxi Shale (Liu et al., 2020b). Compared to the backlimb area, lower porosity in the forelimb might also reduce the impact of young recharge water allowing the preservation of pristine crustal noble gas signatures in some forelimb samples, e.g., N16.

5.2. Diffusion-driven migration of subsurface fluids

In Fig. 6A, $^{20}\mathrm{Ne}/^{22}\mathrm{Ne}$ and $^{21}\mathrm{Ne}/^{22}\mathrm{Ne}$ ratios of some gas samples in this study are plotted along with the corresponding air values. Mixing lines are also shown for the mixing of atmospheric, crustal Ne, and mantle-derived Ne (mantle Ne is assumed to be sourced from the Mid-Ocean Ridge Basalt or MORB). $^{20}\mathrm{Ne}/^{22}\mathrm{Ne}$ and $^{21}\mathrm{Ne}/^{22}\mathrm{Ne}$ ratios of the crustal and mantle endmembers are 0.3 and 0.33, and 13.8 and 0.075, respectively, as summarized in Castro et al. (2009). Forelimb samples roughly fall on the mixing line of air-crust. $^{20}\mathrm{Ne}/^{22}\mathrm{Ne}$ ratios of backlimb samples generally increase from depression to crest. In particular, $^{20}\mathrm{Ne}/^{22}\mathrm{Ne}$ ratios of crest samples H6, H16, and H24 are higher than the corresponding air value of 9.8, which might be caused by the input of mantle Ne or the diffusion-driven fractionation as previously reported in other hydrocarbon-bearing formations, including the Barnett Shale (United States) (Wen et al., 2017), Qinshui Basin (China; Chen et al., 2019), and Jackson Dome CO_2 Deposit (United States; Zhou et al., 2012). The presence of mantle Ne is unlikely and can be excluded in this study given the absence of mantle He as observed in Fig. 3.

Diffusion-driven fractionation is caused by the differentiated diffusion speed of isotopes with different atomic mass. Lighter isotopes diffuse faster than heavier isotopes, e.g., $^{20}\mathrm{Ne} > {}^{22}\mathrm{Ne}$ and He > Ne > Ar > Kr > Xe (Hunt et al., 2012; Lippolt and Weigel, 1988). Therefore, diffusion-driven fractionation is also called mass dependent fractionation (MDF), which can be estimated as follows (Matsumoto et al., 2004; Wen et al., 2017):

$$\left(\frac{i}{j}\right)_{retained} = \left(\frac{i}{j}\right)_{initial} \times f^{\sqrt{M_j/M_i}-1} \tag{7}$$

$$\left(\frac{i}{j}\right)_{escaped} = \left(\frac{i}{j}\right)_{initial} \times \frac{1 - f^{\sqrt{M_j/M_i}-1}}{1 - f} \tag{8}$$

where subscripts *retained*, *escaped* and *initial* refer to the noble gas isotopic ratios (or elemental ratios) in the retained, escaped, and initial phases. i and j represent noble gas isotopes while M_i and M_j represent the mass of isotopes. f stands for the fraction of isotope j in the retained phase. According to Eqs. 7 and 8, an elevated ratio of light isotope/heavy isotope (e.g., $^{20}\mathrm{Ne}/^{22}\mathrm{Ne}$) is predicted in the escaped phase but lowered ratio of light isotope/heavy isotope in the retained phase.

Calculated nobble gas ratios as following Eqs. 7 and 8 are compared to measured noble gas ratios to assess whether and to what extent the diffusion-driven fractionation might have occurred in our gas samples. Predicted $^{20}\mathrm{Ne}/^{22}\mathrm{Ne}$ and $^{21}\mathrm{Ne}/^{22}\mathrm{Ne}$ ratios in the escaped and retained phases are shown in Fig. 6A. It is clear that gas samples H6 and H24 fall close to the predicted MDF line suggesting the presence of diffusion-driven fractionation. Unlike $^{20}\mathrm{Ne}/^{22}\mathrm{Ne}$, $^{38}\mathrm{Ar}/^{36}\mathrm{Ar}$ ratio will decrease in the escaped phase but increase in the retained phase following MDF. In Fig. 6B, gas samples H6, H24, and N9-h17 are located close to the predicted MDF line. For these two samples (i.e., H6 and H24) which are collected from the crest of backlimb region, elevated $^{20}\mathrm{Ne}/^{22}\mathrm{Ne}$ ratios might be at least partly due to the noble gas fractionation caused by the diffusion process.

The other potential explanation for the noble gas signatures observed in Fig. 6A might be that the air-derived noble gas component could have been fractionated prior to mixing with the crustal component, which was previously suggested in the literature (Chen et al., 2019; Zhou et al., 2012). However, as discussed in the following section, the mixing of atmosphere- and crust-derived noble gas endmembers in the Wufeng-Longmaxi Shale in this study predates the fractionation of noble gas from both endmembers. Therefore, we can exclude the possibility of the presence of a fractionated atmospheric component prior to the mixing of air- and crust-derived noble gases in the shale, e.g., fractionated air-derived noble gases originated from injected hydraulic fracturing fluids as observed by Chen et al. (2019).

All gas samples fall above the predicted MDF line in the plot of
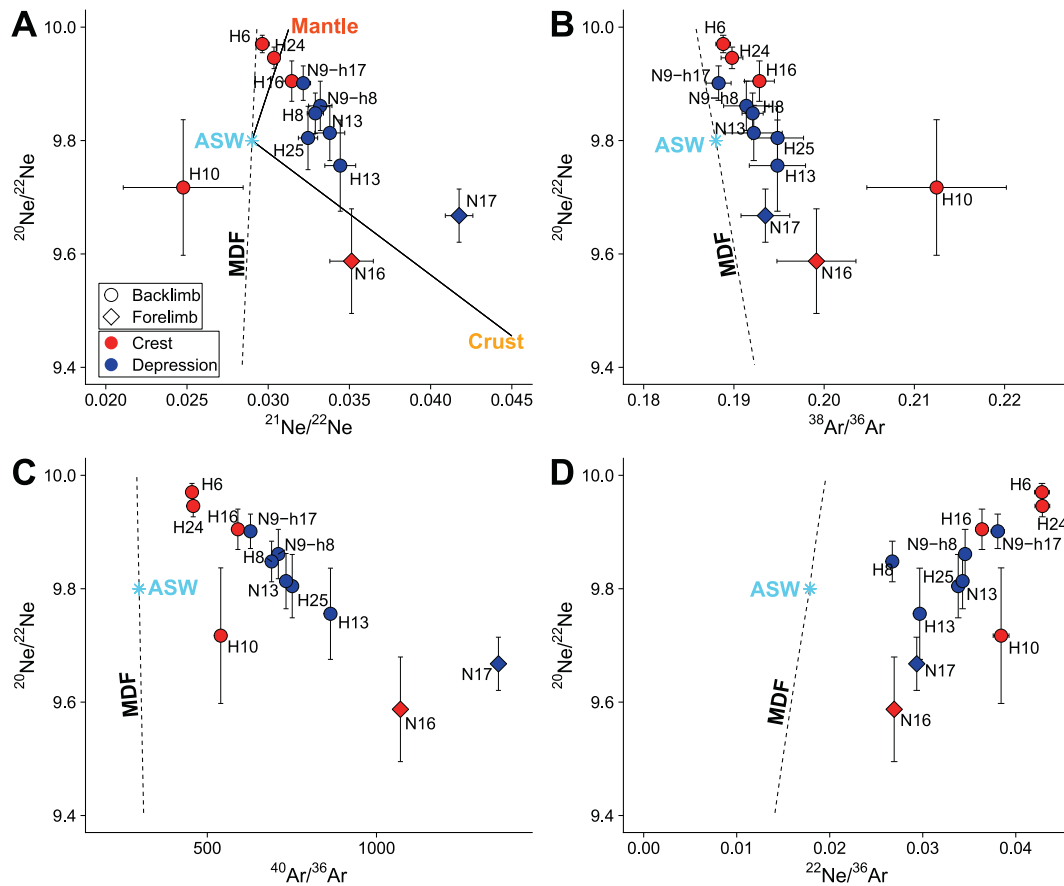
Fig. 6. (A) $^{20}Ne/^{22}Ne$ and $^{21}Ne/^{22}Ne$, (B) $^{20}Ne/^{22}Ne$ and $^{38}Ar/^{36}Ar$, (C) $^{20}Ne/^{22}Ne$ and $^{40}Ar/^{36}Ar$, and (D) $^{20}Ne/^{22}Ne$ and $^{21}Ne/^{36}Ar$ for all gas samples. Typical mixing lines of air-crust and air-mantle (mantle Ne is assumed to be sourced from the Mid-Ocean Ridge Basalt or MORB) are also shown as following Castro et al. (2009). Predicted ratios by following the mass dependent fractionation (MDF) are also shown for comparison. Gas samples with elevated $^{20}Ne/^{22}Ne$ ratio fall close to the predicted MDF lines in (A) and (B) suggesting the presence of diffusion-driven fractionation. All gas samples fall above the predicted MDF line in (C) and (D), pointing to that the impact of MDF on the $^{40}Ar/^{36}Ar$ ratio is negligible compared to the addition of crustal ^{40}Ar and solubility-driven fractionation. Corresponding air values are indicated (Eberhardt et al., 1965; Györe et al., 2019; Mark et al., 2011; Ozima and Podosek, 2002).

$^{20}Ne/^{22}Ne$ and $^{40}Ar/^{36}Ar$ ratios (Fig. 6C), excluding the significant impact of diffusion-driven fractionation on $^{40}Ar/^{36}Ar$ values. As mentioned in section 5.1.3, high $^{40}Ar/^{36}Ar$ ratios of our gas samples are mainly caused by the addition of crustal Ar.

The migration of hydrocarbon gas from the deep depression to the shallow crest in the Wufeng-Longmaxi Shale over geologic time has been previously suggested, for which diffusion is likely the key mechanism of such gas migration given the inherently low permeability of shale (Guo, 2016; Huang et al., 2020). The above discussion in this section argues that diffusion-driven fractionation has likely occurred to varying extents in gas samples from the crest and depression, which might imply a diffusion-governing long-distance migration of hydrocarbon and noble gases in the shale, from the depression at a greater depth to the shallow crest. Towards crest samples, a longer distance of migration might lead to greater diffusion-driven fractionation resulting in further elevated $^{20}Ne/^{22}Ne$ ratios in crest samples including H6, H16, and H24.

5.3. Multi-phase interactions of water, oil, and gas

Noble gas elemental ratio (e.g., $^{22}Ne/^{36}Ar$) can be altered not only by diffusion-driven fractionation but also by the solubility-driven fractionation. Because the solubility of noble gases in water and oil increases with the atomic mass: He < Ne < Ar < Kr < Xe (Weiss, 1971a, 1971b), light noble gases (e.g., ^{22}Ne) thus will be preferentially enriched in the gas phase when a gas phase is stripping a water phase, leading to an elevated elemental ratio of light to heavy noble gases (e.g., $^{22}Ne/^{36}Ar$

ratio) in the gas phase and a lowered ratio in the retained water phase (Ballentine et al., 1991; Battani et al., 2000; Wen et al., 2015, 2017). In Fig. 6D, all gas samples fall above the MDF line, pointing to that the impact of MDF on the elemental ratios is negligible compared to solubility-driven fractionation (see Supplementary Material for details).

To explain measured high $^{22}Ne/^{36}Ar$ ratios in our gas samples, by assuming the solubility-driven fractionation is single-stage in a two-phase system (i.e., gas and water), noble gas elemental ratios can be calculated as follows (Ballentine et al., 2002):

$$\left(\frac{i}{j}\right)_{gas} = \left(\frac{i}{j}\right)_{initial} \frac{1 - f_1^{\alpha_1}}{1 - f_1} \quad (9)$$

where subscripts *gas* and *initial* refer to the noble gas elemental ratios in the escaped gas phase and the initial water phase (e.g., ASW), *i* and *j* represent noble gas isotopes (e.g., ^{22}Ne, ^{36}Ar), f_1 stands for the fraction of isotope *j* remained in the retained water phase. The coefficient α_1 is defined by:

$$\alpha_1 = K_i^{water} \Big/ K_j^{water} \quad (10)$$

where K_i^{water} and K_j^{water} represent Henry constants of isotopes *i* and *j* in water (Table S1). As the volume ratio of gas/water approaches 0, the fractionation is maximum:

$$\left(\frac{i}{j}\right)_{gas} = \left(\frac{i}{j}\right)_{initial} \alpha_1 \quad (11)$$

Measured $^{22}Ne/^{36}Ar$, $^{84}Kr/^{36}Ar$, and $^{132}Xe/^{36}Ar$ ratios are shown for all gas samples (Fig. 7), along with predicted noble gas ratios in the escaped gas phase for 25 °C and 90 °C. Although this single-stage model can well explain measured $^{22}Ne/^{36}Ar$ values, it fails to account for most of $^{84}Kr/^{36}Ar$ and $^{132}Xe/^{36}Ar$ measurements (e.g., N17, H8, and H25; see Supplementary Material for details), for which alternative models are needed.

One of the viable models is a two-stage fractionation model of groundwater gas stripping and re-dissolution (GGSR; Fig. 7) (Gilfillan et al., 2008; Zhou et al., 2012). This GGSR model involves the re-dissolution of the gas phase that initially is stripped from a water phase into the other (or the same) water phase. This re-dissolution can be caused by the change in reservoir conditions. The gas phase initially generated by water degassing will have higher $^{22}Ne/^{36}Ar$ but lower $^{84}Kr/^{36}Ar$ (and $^{132}Xe/^{36}Ar$) ratios. As re-dissolving into the water phase, $^{84}Kr/^{36}Ar$ (and $^{132}Xe/^{36}Ar$) ratios in the retained gas phase will further decrease. GGSR model combined with the addition of atmospheric Xe and Kr sourced from the organic matter (Kennedy et al., 2002) can explain observed noble gas signatures in most gas samples, except for samples H8 and N17 with extremely low $^{84}Kr/^{36}Ar$. In addition, neither the single-stage gas-water separation model nor the two-stage GGSR model takes the oil phase into account, whereas the presence of an oil phase over geological time is an integral part of the Wufeng-Longmaxi Shale (Dai et al., 2014). An alternative viable model considering the past presence of oil phase to explain the observed noble gas signatures, in particular low $^{84}Kr/^{36}Ar$ values in some samples in the Wufeng-Longmaxi Shale, can be the two-stage oil modified water exsolution (OMGE) fractionation model (Battani et al., 2000).

In the OMGE model, noble gas fractionation occurs in two stages: 1) noble gases that are initially in the water phase will be fractionated after the water phase gets in contact with an oil phase, and 2) the water phase with modified noble gas signatures will then get through further noble gas fractionation when the water phase subsequently is in equilibrium with a gas phase. Noble gas elemental ratios in the water phase after the first stage 1 can be calculated by Battani et al. (2000):

$$\left(\frac{i}{j}\right)_{water} = \left(\frac{i}{j}\right)_{initial} f_2^{(\alpha_2-1)} \tag{12}$$

where f_2 is the fraction of j in the retained water phase, the α_2 is defined by:

$$\alpha_2 = \left(K_i^{water} \middle/ K_j^{water}\right) \middle/ \left(K_i^{oil} \middle/ K_j^{oil}\right) \tag{13}$$

where K_i^{oil} and K_j^{oil} are Henry constants of i and j in oil (Table S1; light oil phase with an API = 34). The noble gas fractionation in stage 2 can be modeled by the above Eqs. 9–11. Noble gas elemental ratio in the final escaped gas phase can be estimated by:

$$\left(\frac{i}{j}\right)_{gas} = \left(\frac{i}{j}\right)_{initial} f_2^{(\alpha_2-1)} \left(\frac{1-f_1^{\alpha_1}}{1-f_1}\right) \tag{14}$$

Predicted $^{22}Ne/^{36}Ar$, $^{84}Kr/^{36}Ar$, and $^{132}Xe/^{36}Ar$ ratios by assuming that stage 1 occurs under 150 °C, the temperature of which is representative for the main period of oil generation at a vitrinite reflectance of approximately 1.0 in the Wufeng-Longmaxi Shale (Gao et al., 2017; Liu et al., 2020c), and stage 2 takes place under 90 °C are shown as dotted-dashed curves in Fig. 7. The addition of various amounts of atmospheric Kr and Xe is also considered (Fig. 7A and B) (Kennedy et al., 2002). It is clear that measured $^{22}Ne/^{36}Ar$, $^{84}Kr/^{36}Ar$, and $^{132}Xe/^{36}Ar$ values of gas samples in this study can be well explained by the OMGE model with the addition of atmospheric Kr and Xe up to 1250% and 1550% of the Kr and Xe contents in the original ASW phase, respectively. The match between OMGE model results and the observed noble gas signatures, in turn, supports the past presence of an oil phase in the Wufeng-Longmaxi Shale.

As mentioned above, radiogenic noble gases (e.g., $^{40}Ar_{rad}$) in the Wufeng-Longmaxi Shale are likely originated from an external source from the deeper crust. In Fig. 8A, calculated $^4He_{rad}/^{40}Ar_{rad}$ and measured $^{22}Ne/^{36}Ar$ ratios, which are normalized by the average $^4He_{rad}/^{40}Ar_{rad}$ ratio of 5.7 of crust (Ballentine and Burnard, 2002) and $^{22}Ne/^{36}Ar$ ratio in ASW at 25 °C, are plotted for all gas samples. In general, gas samples show a positive correlation (although not fall on the line of 1:1 exactly) between the normalized $^4He_{rad}/^{40}Ar_{rad}$ and $^{22}Ne/^{36}Ar$ values, implying a coherent fractionation of the atmosphere-derived (e.g., ^{22}Ne and ^{36}Ar) and radiogenic (e.g., $^4He_{rad}$ and $^{40}Ar_{rad}$) noble gases during groundwater degassing. To make the normalized ratios fall on the line of 1:1, calculated $^4He_{rad}/^{40}Ar_{rad}$ ratios need to be normalized by a crustal value of 4.5 (Fig. 8B). This lower $^4He_{rad}/^{40}Ar_{rad}$ ratio of 4.5 is within the range of $^4He_{rad}/^{40}Ar_{rad}$ ratios for the lower and
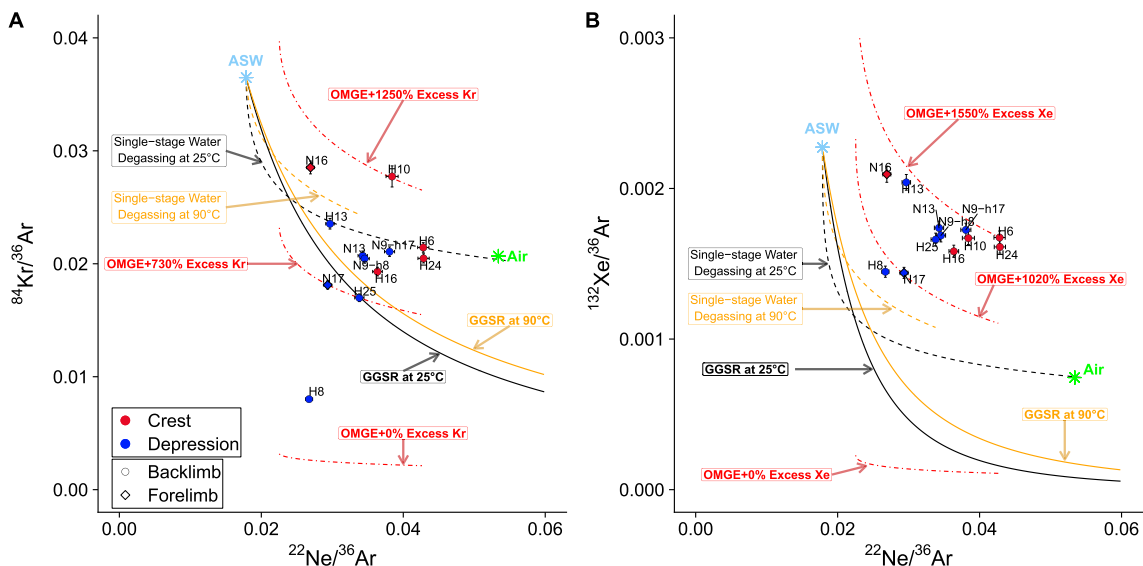
Fig. 7. (A) $^{84}Kr/^{36}Ar$ versus $^{22}Ne/^{36}Ar$ and (B) $^{132}Xe/^{36}Ar$ versus $^{22}Ne/^{36}Ar$ are shown for the gas samples in this study. Predicted values in the gas phase following a single-stage groundwater degassing model for an open system (dashed curves) under 25 °C and 90 °C are shown. Calculated values in the gas phase following the groundwater gas stripping and re-dissolution (GGSR) model and oil-modified groundwater exsolution (OMGE) model with various amounts of sedimentary noble gas under 25 °C and 90 °C are also shown (solid and dotted-dashed curves, respectively).
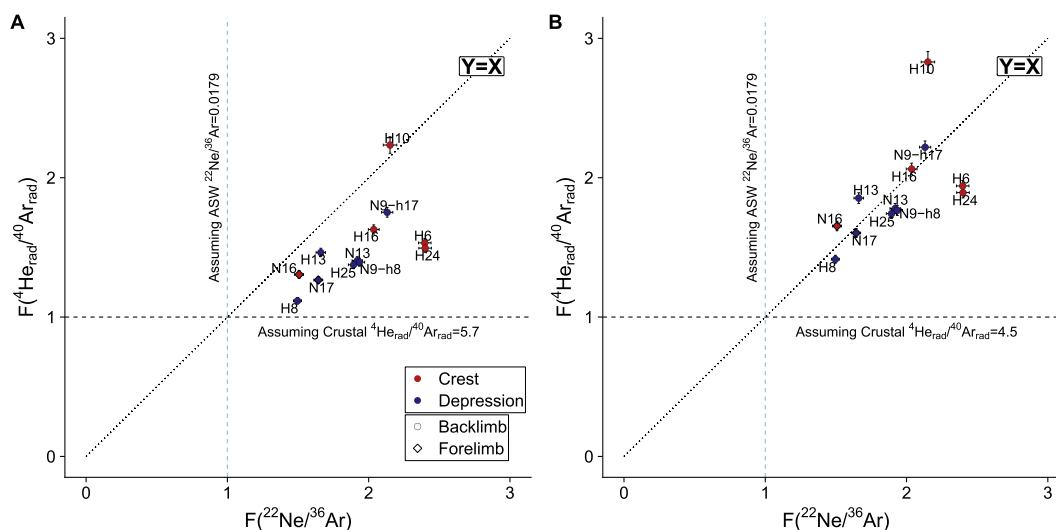
Fig. 8. Cross plot of normalized $^4He_{rad}/^{40}Ar_{rad}$ and $^{22}Ne/^{36}Ar$ ratios for two scenarios. (A) the $^4He_{rad}/^{40}Ar_{rad}$ ratio is normalized the average ratio $^4He_{rad}/^{40}Ar_{rad}$ in the crust while $^{22}Ne/^{36}Ar$ value is normalized to the ASW value at 25 °C (Ozima and Podosek, 2002). (B) $^{22}Ne/^{36}Ar$ value is still normalized to the ASW value at 25 °C while $^4He_{rad}/^{40}Ar_{rad}$ ratio is normalized to an optimal $^4He_{rad}/^{40}Ar_{rad}$ value of 4.5 so that most samples fall on the line of 1:1.

upper crust: 3.09–6.0 (Ballentine and Burnard, 2002). The observed correlation suggests that the noble gas fractionation likely postdates the mixing of atmosphere-derived and radiogenic noble gases in the Wufeng-Longmaxi Shale.

5.4. Temporal development of reservoir compartmentalization triggered by tectonic deformation

The reservoir compartmentalization observed in the Wufeng-Longmaxi Shale is likely caused by the interactions of multi-phase subsurface fluid, which in turn is modulated by the tectonic deformation over geologic time. To constrain the timing of emergence and development of shale reservoir compartmentalization, we further calculate the accumulation time of $^4He_{rad}$ content (Ballentine and Burnard, 2002; Wen et al., 2015; Torgersen, 1980; Zhou et al., 2012), which refers to the time required for each sample to reach the amount of $^4He_{rad}$ measured. Detailed steps of calculating the accumulation time are included in the Supplementary Material (Eqs. S1 to S4).

The ^4He accumulation time for all gas samples is calculated for both closed and open systems. For a closed system, calculated ^4He accumulation time of our gas samples generally ranges from approximately 8 to 46 Ma (Table 4), which are far less than the shale deposition age of approximately 445 to 440 Ma (i.e., from Late Ordovician to Early Silurian) (Fig. S1). A few samples (e.g., N17) present a ^4He accumulation time close to or even older than the age of major tectonic exhumation [~45 Ma; this is revealed by the dating analysis of apatite fission track in the Changning area (He et al., 2018)] during which the majority of accumulated crustal noble gases are assumed to be expulsed *a priori*. Therefore, an external source of crustal He has likely migrated into the Wufeng-Longmaxi Shale following the tectonic exhumation to recharge the He accumulation to be able to account for the radiogenic He contents currently observed in our gas samples. Considering an external ^4He flux originated from the underlying crust, (i.e., an open system), the calculated ^4He accumulation time has largely decreased to <1 Ma (Table 4). Forelimb samples, N16 and N17, present ^4He accumulation ages older than most or all backlimb samples in both closed and open systems. These observations combined suggest that a higher flux of external ^4He from the underlying crust following the major tectonic exhumation might be present in the forelimb compared to the backlimb.

As a summary, it is likely that subsurface fluids in the Wufeng-Longmaxi Shale and the deeper crust might have gone through a multi-stage process. In particular, prior to the tectonic exhumation, the

Table 4
Calculated ^4He groundwater age of shale gas samples in the Changning area in the Sichuan Basin[a, b, c, d].

Well	$^4He/^{36}Ar$	$^4He_{water}$	ω	In-situ $^4He_{age}$	External $^4He_{age}$
		($\times 10^{-3}$ cm^3 STP g$^{-1}_{H2O}$)	(%)	(Ma)	(Ma)
N16	5710	4.77	4	34.82	0.17
H10	3080	2.57	6	28.77	0.14
H16	2709	2.26	6	25.31	0.12
H24	1374	1.15	6	8.38	0.04
H6	1376	1.15	6	12.86	0.06
N17	7607	6.36	4	46.38	0.22
H13	4696	3.92	6	43.86	0.21
N9-h17	3280	2.74	6	30.67	0.14
N9-h8	3256	2.72	6	30.45	0.14
N25	3531	2.95	6	33.02	0.16
N13	3464	2.90	6	32.37	0.15
H8	2484	2.08	6	23.23	0.11

[a] $^{36}Ar_{ASW} = 8.36 \times 10^{-7}$ (the seawater with a salinity of 0.6 M in equilibrium with the air at 25 °C) (Ozima and Podosek, 2002).
[b] The ^4He production rate (in cm^3 STP/g$_{rock}$/yr), density (in g/cm^3), and thickness (in m) of the upper and lower crust are 6.45 × 10^{-13}, 2.6, 12,300, and 6.42 × 10^{-14}, 3.3, 36,900, respectively (Wen et al., 2015; Zhou and Ballentine, 2006).
[c] U and Th concentrations in the Wufeng-Longmaxi Shale are 15 and 12 ppm, respectively.
[d] The average thickness of Wufeng-Longmaxi Shale is assumed to be 25 m.

accumulation of crustal noble gases in addition to the preservation of atmospheric noble gases from the original recharge seawater continued. In the meantime, the interaction of oil and water phases was likely initiated since ~200 Ma (Fig. 9) (Liu et al., 2020c), i.e., the start of the major time period of oil generation, leading to noble gas fractionation as described by the first stage of the OMGE model. As massive hydrocarbon gas was generated by the cracking of oil since ~150 Ma (Liu et al., 2020c), the noble gas fractionation driven by the multi-phase interaction of gas-water-oil was also triggered. Following the tectonic movements that occurred at ~45 Ma, basement-involved faults were generated particularly in the forelimb area. In addition, the basement-involved faulting activities also contributed to the porosity reduction due to the pore collapse especially in the forelimb area. The presence of
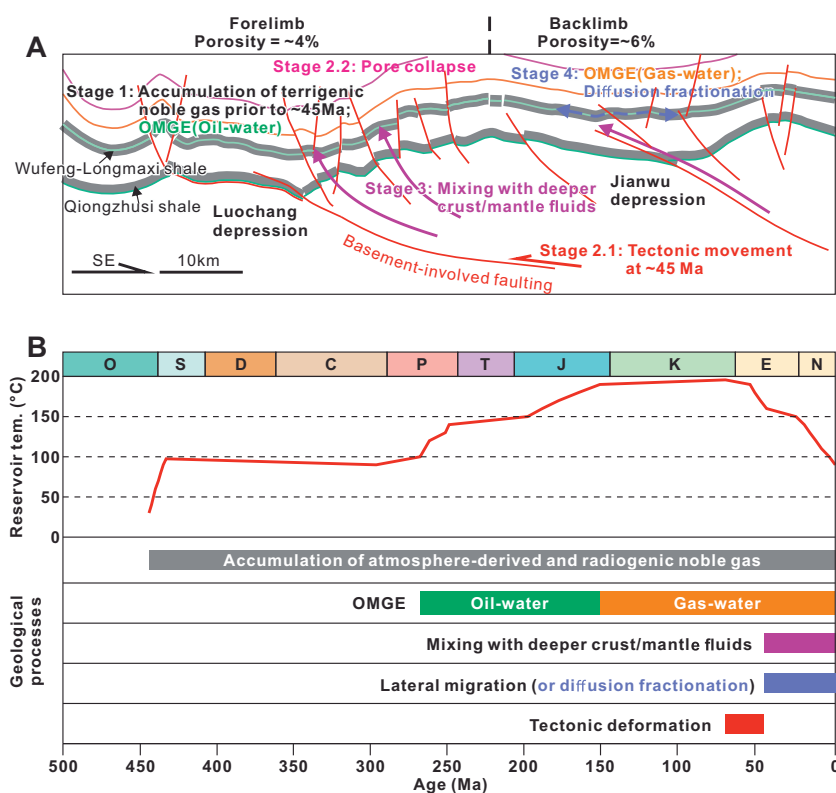
Fig. 9. (A) Schematic illustration showing the mechanisms of spatiotemporal variability of noble gas signatures in the Wufeng-Longmaxi Shale of the Changning area. Stage 1: before tectonic deformation, the accumulation of terrigenic noble gases in addition to the preservation of atmospheric noble gases continues in the Wufeng-Longmaxi Shale. Oil-water interactions (i.e., the former part of the OMGE model) cause noble gas fractionation. Stage 2: Tectonic movements occur at ~45 Ma which leads to the porosity reduction especially in the forelimb area due to the pore collapse. Stage 3: the basement-involved faults facilitate the migration of subsurface fluids from the deep crust into the Wufeng-Longmaxi Shale. Stage 4: after tectonic deformation, gas-water interactions as described by the latter part of the OMGE model cause fractionation in both atmospheric and crustal noble gases. (B) A diagram showing the timing and temporal span of the relevant geological process as well as the reconstructed reservoir temperature in the Wufeng-Longmaxi Shale as modified from (Liu et al., 2020c).

deep faults facilitated the migration of subsurface fluids from the deep crust into the Wufeng-Longmaxi Shale. Following the mixing of the subsurface fluids from deeper formations and fluids within the shale, with the diminishment of oil phase in the shale, the fractionation of both atmospheric and crustal noble gases in the shale was mostly governed by the water-gas interaction as described by the second stage of the OMGE model. With the accumulation of hydrocarbon gas, the long-distance migration governed by the diffusion from depression to crest was also triggered leading to further fractionated noble gas ratios particularly in the crest samples. Compared to the backlimb area, lower porosity in the forelimb area allows a better preservation of subsurface fluids with less impact from younger recharge water into the shale. This four-stage process is illustrated in Fig. 9 to explain the observed dichotomous patterns in noble gas signatures between forelimb and backlimb regions, and crest and depression samples.

6. Conclusions

This study presents measurements of the bulk gas composition, carbon and hydrogen stable isotope, and noble gas volume fraction and isotope for shale gas samples collected from twelve unconventional gas wells that tap into the Wufeng-Longmaxi Shale in the Changning area, the southern Sichuan Basin, China.

In all well-preserved gas samples, CH_4 is the dominant gas, with stable carbon and hydrocarbon isotopic ratios $\delta^{13}C_1$ and δDC_1 varying from −28.8 to −27.3‰ and − 153 to −145‰, respectively, indicating a late mature thermogenic origin gas.

$^3He/^4He$ ratios of the gas samples are almost constant around $0.01R_A$ (R_A denotes $^3He/^4He$ ratio in the air) suggesting a dominantly crustal He. $^{21}Ne/^{22}Ne$ and $^{40}Ar/^{36}Ar$ ratios of many gas samples are higher than the corresponding air values pointing to the mixing of crustal and atmospheric noble gases. In addition, forelimb wells present the highest $^{21}Ne/^{22}Ne$ and $^{40}Ar/^{36}Ar$ ratios indicating larger flux/contribution of crustal noble gas in these wells. Elemental ratios of atmospheric noble gas isotopes – $^{22}Ne/^{36}Ar$, $^{84}Kr/^{36}Ar$, and $^{132}Xe/^{36}Ar$ are compared to the

corresponding values in the initial recharge water (ASW): $^{22}Ne/^{36}Ar$ ratios of all gas samples are higher than the corresponding ASW ratio while $^{84}Kr/^{36}Ar$ and $^{132}Xe/^{36}Ar$ ratios are lower than the ASW values. Considering that oil phase is an integral part of the history of the Wufeng-Longmaxi, to explain extremely low $^{84}Kr/^{36}Ar$ ratios in some samples, a two-stage model of noble gas fractionation that involves gas, water, and oil phases is adopted, in which the formation water first is in contact with the oil phase before getting in equilibrium with the hydrocarbon gas phase originated from the oil cracking. Calculated groundwater ages based on the radiogenic ^4He contents in the gas samples also require that the Wufeng-Longmaxi Shale is an open system with an external flux of subsurface fluid from the deeper crust. Gas samples collected from the forelimb area generally display ages older than backlimb samples, likely indicating a larger flux of external ^4He due to the higher density of deep faults in the forelimb area caused by the basement-involved deformation. In the meantime, the basement-involved deformation also causes the pore collapse especially in the forelimb leading to a lower porosity compared to the backlimb. This in turn allows a better preservation of noble gases in the shale by reducing the recharge of younger groundwater into the shale.

Declaration of Competing Interest

The authors declare that they have no known competing financial interests or personal relationships that could have appeared to influence the work reported in this paper.

Acknowledgments

operators at PetroChina for sampling assistance. We would also like to thank the editor for handling this article and the constructive comments from anonymous reviewers.

Appendix A. Supplementary data

References

Ballentine, C.J., Burnard, P.G., 2002. Production, release and transport of noble gases in the continental crust. In: Porcelli, D.R., Ballentine, C.J., Weiler, R. (Eds.), Reviews in Mineralogy & Geochemistry, 47, Noble Gases in Geochemistry and Cosmochemistry, pp. 481–538. https://doi.org/10.2138/rmg.2002.47.12.

Ballentine, C.J., O'Nions, R.K., Oxburgh, E.R., Horvath, F., Deak, J., 1991. Rare gas constraints on hydrocarbon accumulation, crustal degassing and groundwater flow in the Pannonian Basin. Earth Planet. Sci. Lett. 105, 229–246. https://doi.org/10.1016/0012-821X(91)90133-3.

Ballentine, C.J., Burgess, R., Marty, B., 2002. Tracing fluid origin, transport and interaction in the crust. In: Porcelli, D.R., Ballentine, C.J., Weiler, R. (Eds.), Reviews in Mineralogy & Geochemistry, 47, Noble Gases in Geochemistry and Cosmochemistry, pp. 539–614. https://doi.org/10.2138/rmg.2002.47.13.

Barry, P.H., Lawson, M., Meurer, W.P., Warr, O., Mabry, J.C., Byrne, D.J., Ballentine, C. J., 2016. Noble gases solubility models of hydrocarbon charge mechanism in the Sleipner Vest gas field. Geochim. Cosmochim. Acta 194, 291–309. https://doi.org/10.1016/j.gca.2016.08.021.

Battani, A., Sarda, P., Prinzhofer, A., 2000. Basin scale natural gas source, migration and trapping traced by noble gases and major elements: the Pakistan Indus basin. Earth Planet. Sci. Lett. 181, 229–249. https://doi.org/10.1016/s0012-821x(00)00188-6.

Byrne, D.J., Barry, P.H., Lawson, M., Ballentine, C.J., 2018. Determining gas expulsion vs retention during hydrocarbon generation in the Eagle Ford Shale using noble gases. Geochim. Cosmochim. Acta 241, 240–254. https://doi.org/10.1016/j.gca.2018.08.042.

Byrne, D.J., Barry, P.H., Lawson, M., Ballentine, C.J., 2020. The use of noble gas isotopes to constrain subsurface fluid flow and hydrocarbon migration in the East Texas Basin. Geochim. Cosmochim. Acta 268, 186–208. https://doi.org/10.1016/j.gca.2019.10.001.

Cao, C., Zhang, M., Tang, Q., Yang, Y., Lv, Z., Zhang, T., Chen, C., Yang, H., Li, L., 2018. Noble gas isotopic variations and geological implication of Longmaxi shale gas in Sichuan Basin, China. Mar. Pet. Geol. 89, 38–46. https://doi.org/10.1016/j.marpetgeo.2017.01.022.

Castro, M.C., Ma, L., Hall, C.M., 2009. A primordial, solar He–Ne signature in crustal fluids of a stable continental region. Earth Planet. Sci. Lett. 279, 174–184. https://doi.org/10.1016/j.epsl.2008.12.042.

Chen, B., Stuart, F.M., Xu, S., Györe, D., Liu, C., 2019. Evolution of coal-bed methane in Southeast Qinshui Basin, China: Insights from stable and noble gas isotopes. Chem. Geol. 529, 119298. https://doi.org/10.1016/j.chemgeo.2019.119298.

China National Petroleum Corporation, 2020. Daily Shale Gas Production in Changning Field Ranks First in China (in Chinese). CNPC Press. http://news.cnpc.com.cn/system/2020/10/12/030012499.shtml.

Clarke, W.B., Jenkins, W.J., Top, Z., 1976. Determination of tritium by mass spectrometric measurement of 3He. Int. J. Appl. Radiat. Isotopes 27, 515–522.

Dai, J., Zou, C., Liao, S., Dong, D., Ni, Y., Huang, J., Wu, W., Gong, D., Huang, S., Hu, G., 2014. Geochemistry of the extremely high thermal maturity Longmaxi shale gas, southern Sichuan Basin. Org. Geochem. 74, 3–12. https://doi.org/10.1016/j.orggeochem.2014.01.018.

Darrah, T.H., Vengosh, A., Jackson, R.B., Warner, N.R., Poreda, R.J., 2014. Noble gases identify the mechanisms of fugitive gas contamination in drinking-water wells overlying the Marcellus and Barnett Shales. Proc. Natl. Acad. Sci. U. S. A. 111, 14076–14081. https://doi.org/10.1073/pnas.1322107111.

Darrah, T.H., Jackson, R.B., Vengosh, A., Warner, N.R., Whyte, C.J., Walsh, T.B., Kondash, A.J., Poreda, R.J., 2015. The evolution of Devonian hydrocarbon gases in shallow aquifers of the northern Appalachian Basin: Insights from integrating noble gas and hydrocarbon geochemistry. Geochim. Cosmochim. Acta 170, 321–355. https://doi.org/10.1016/j.gca.2015.09.006.

Eberhardt, P., Eugster, O., Marti, K., 1965. Notizen: a redetermination of the isotopic composition of atmospheric neon. Zeitschrift für Naturforschung A 20, 623–624. https://doi.org/10.1515/zna-1965-0420.

English, K.L., English, J.M., Redfern, J., Hollis, C., Corcoran, D.V., Oxtoby, N., Cherif, R. N., 2016. Remobilization of deep basin brine during exhumation of the Illizi Basin, Algeria. Mar. Pet. Geol. 78, 679–689. https://doi.org/10.1016/J.MARPETGEO.2016.08.016.

Gao, J., He, S., Zhao, J.X., Yi, J., 2017. Geothermometry and geobarometry of overpressured lower Paleozoic gas shales in the Jiaoshiba field, Central China: insight from fluid inclusions in fracture cements. Mar. Pet. Geol. 83, 124–139.

Gilfillan, S.M.V., Ballentine, C.J., Holland, G., Blagburn, D., Sherwood Lollar, B., Stevens, S., Schoell, M., Cassidy, M., 2008. The noble gas geochemistry of natural CO2 gas reservoirs from the Colorado Plateau and Rocky Mountain provinces, USA. Geochim. Cosmochim. Acta 72, 1174–1198. https://doi.org/10.1016/j.gca.2007.10.009.

Gilfillan, S.M.V., Györe, D., Flude, S., Johnson, G., Bond, C.E., Hicks, N., Lister, R., Jones, D.G., Kremer, Y., Haszeldine, R.S., Stuart, F.M., 2019. Noble gases confirm

plume-related mantle degassing beneath Southern Africa. Nat. Commun. 10, 5028. https://doi.org/10.1038/s41467-019-12944-6.

Graham, D.W., 2002. Noble gas isotope geochemistry of mid-ocean ridge and ocean island basalts: characterization of mantle source reservoirs. Rev. Mineral. Geochem. 47, 247–317. https://doi.org/10.2138/rmg.2002.47.8.

Guo, T., 2016. Key geological issues and main controls on accumulation and enrichment of Chinese shale gas. Petrol. Explor. Develop. 43, 317–326. https://doi.org/10.1016/S1876-3804(16)30042-8.

Györe, D., Stuart, F.M., Gilfillan, S.M.V., Waldron, S., 2015. Tracing injected CO2 in the Cranfield enhanced oil recovery field (MS, USA) using He, Ne and Ar isotopes. Int. J. Greenh. Gas Control 42, 554–561. https://doi.org/10.1016/j.ijggc.2015.09.009.

Györe, D., McKavney, R., Gilfillan, S.M.V., Stuart, F.M., 2018. Fingerprinting coal-derived gases from the UK. Chem. Geol. 480, 75–85. https://doi.org/10.1016/j.chemgeo.2017.09.016.

Györe, D., Tait, A., Hamilton, D., Stuart, F.M., 2019. The formation of NeH+ in static vacuum mass spectrometers and re-determination of 21Ne/20Ne of air. Geochim. Cosmochim. Acta 263, 1–12. https://doi.org/10.1016/j.gca.2019.07.059.

Györe, D., Pujol, M., Gilfillan, S.M.V., Stuarta, F.M., 2021. Noble gases constrain the origin, age and fate of CO2 in the Vaca Muerta Shale in the Neuqu'en Basin (Argentina). Chem. Geol. 577, 120294. https://doi.org/10.1016/j.chemgeo.2021.120294.

Hao, F., Zou, H., 2013. Cause of shale gas geochemical anomalies and mechanisms for gas enrichment and depletion in high-maturity shales. Mar. Pet. Geol. 44, 1–12. https://doi.org/10.1016/j.marpetgeo.2013.03.005.

Hao, F., Zou, H.Y., Lu, Y.C., 2013. Mechanisms of shale gas storage: Implications for shale gas exploration in China. AAPG Bull. 97, 1325–1346. https://doi.org/10.1306/02141312091.

Harkness, J.S., Darrah, T.H., Warner, N.R., Whyte, C.J., Moore, M.T., Millot, R., Kloppmann, W., Jackson, R.B., Vengosh, A., 2017. The geochemistry of naturally occurring methane and saline groundwater in an area of unconventional shale gas development. Geochim. Cosmochim. Acta 208, 302–334. https://doi.org/10.1016/j.gca.2017.03.039.

He, W., Zhou, J., Yuan, K., 2018. Deformation evolution of Eastern Sichuan–Xuefeng fold-thrust belt in South China: Insights from analogue modelling. J. Struct. Geol. 109, 74–85. https://doi.org/10.1016/j.jsg.2018.01.002.

Huang, C., Zhang, F., Li, S., Yang, Z., Zhang, X., Hu, P., Tong, S., 2020. Analysis and application of gas migration mechanism within shale. Sci. Technol. Eng. 20, 6752–6759 (in Chinese with English abstract).

Hunt, A.G., Darrah, T.H., Poreda, R.J., 2012. Determining the source and genetic fingerprint of natural gases using noble gas geochemistry: a northern Appalachian Basin case study. AAPG Bull. 96, 1785–1811. https://doi.org/10.1306/03161211093.

Karolytè, R., Johnson, G., Györe, D., Serno, S., Flude, S., Stuart, F.M., Chivas, A.R., Boyce, A., Gilfillan, S.M.V., 2019. Tracing the migration of mantle CO2 in gas fields and mineral water springs in south-East Australia using noble gas and stable isotopes. Geochim. Cosmochim. Acta 259, 109–128. https://doi.org/10.1016/j.gca.2019.06.002.

Kennedy, B.M., Torgersen, T., van Soest, M.C., 2002. Multiple atmospheric noble gas components in hydrocarbon reservoirs: a study of the Northwest Shelf, Delaware Basin, SE New Mexico. Geochim. Cosmochim. Acta 66, 2807–2822. https://doi.org/10.1016/S0016-7037(02)00883-9.

Larter, S.R., Bowler, B.F.J., Li, M., Chen, M., Brincat, D., Bennett, B., Noke, K., Donohoe, P., Simmons, D., Kohnen, M., Allan, J., Telnaes, N., Horstad, I., 1996. Molecular indicators of secondary oil migration distances. Nature 383, 593–597. https://doi.org/10.1038/383593a0.

Lee, J.Y., Marti, K., Severinghaus, J.P., Kawamura, K., Yoo, H.S., Lee, J.B., Kim, J.S., 2006. A redetermination of the isotopic abundances of atmospheric Ar. Geochim. Cosmochim. Acta 70, 4507–4512. https://doi.org/10.1016/j.gca.2006.06.1563.

Li, Y., Qin, S., Wang, Y., Holland, G., Zhou, Z., 2020. Tracing interaction between hydrocarbon and groundwater systems with isotope signatures preserved in the Anyue gas field, Central Sichuan Basin, China. Geochim. Cosmochim. Acta 274, 261–285. https://doi.org/10.1016/j.gca.2020.01.039.

Lippolt, H.J., Weigel, E., 1988. 4He diffusion in 40Ar-retentive minerals. Geochim. Cosmochim. Acta 52, 1449–1458. https://doi.org/10.1016/0016-7037(88)90215-3.

Liu, R., Hao, F., Engelder, T., Shu, Z., Yi, J., Xu, S., Teng, C., 2019. Stress memory extracted from shale in the vicinity of a fault zone: Implications for shale-gas retention. Mar. Pet. Geol. 102, 340–349. https://doi.org/10.1016/j.marpetgeo.2018.12.047.

Liu, R., Hao, F., Engelder, T., Shu, Z., Yi, J., Xu, S., Teng, C., 2020a. Influence of tectonic exhumation on porosity of Wufeng–Longmaxi shale in the Fuling gas field of the eastern Sichuan Basin, China. AAPG Bull. 104, 939–959. https://doi.org/10.1306/08161918071.

Liu, R., Zheng, J., Hao, F., Nie, Z., Heng, D., Tan, X., Jiang, D., 2020b. Variation in pore systems with tectonic stress in the overthrust Wufeng-Longmaxi shale of the southern Sichuan Basin, China. J. Nat. Gas Sci. Eng. 83, 103617. https://doi.org/10.1016/j.jngse.2020.103617.

Liu, W., Zhou, Z., Wu, J., Luo, C., Wu, W., Jiang, L., Jiao, K., Ye, Y., Deng, B., 2020c. Hydrocarbon generation and shale gas accumulation in the Wufeng-Longmaxi formations, Changning shale-gas field, Southern Sichuan Basin. J. Nanjing Univ. (Nat. Sci.) 56, 393–404 (in Chinese with English abstract). 10.13232/j.cnki.jnju.2020.03.008.

Ma, L., Castro, M.C., Hall, C.M., 2009. Atmospheric noble gas signatures in deep Michigan Basin brines as indicators of a past thermal event. Earth Planet. Sci. Lett. 277, 137–147. https://doi.org/10.1016/j.epsl.2008.10.015.

Mark, D.F., Stuart, F.M., de Podesta, M., 2011. New high-precision measurements of the isotopic composition of atmospheric argon. Geochim. Cosmochim. Acta 75, 7494–7501. https://doi.org/10.1016/j.gca.2011.09.042.

Matsumoto, T., Honda, M., McDougall, I., Yatsevich, I., O'Reilly, S.Y., 2004. Isotope fractionation of neon during stepheating extraction?: a comment on 'Re-interpretation of the existence of a primitive plume under Australia based on neon isotope fractionation during step heating' by Gautheron and Moreira (2003). Terra Nova 16, 23–26. https://doi.org/10.1046/j.1365-3121.2003.00522.x.

Meng, Q.R., Wang, E., Hu, J.M., 2005. Mesozoic sedimentary evolution of the Northwest Sichuan basin: Implication for continued clockwise rotation of the South China block. Geol. Soc. Am. Bull. 117, 396–410. https://doi.org/10.1130/b25407.1.

Milkov, A.V., Faiz, M., Etiope, G., 2020. Geochemistry of shale gases from around the world: Composition, origins, isotope reversals and rollovers, and implications for the exploration of shale plays. Org. Geochem. 143, 103997. https://doi.org/10.1016/j.orggeochem.2020.103997.

Mishima, K., Sumino, H., Yamada, T., Ieki, S., Nagakura, N., Otono, H., Oide, H., 2018. Accurate determination of the absolute ^{3}He/^{4}He ratio of a synthesized helium standard gas (helium standard of Japan, HESJ): toward revision of the atmospheric ^{3}He/^{4}He ratio. Geochem. Geophys. Geosyst. 19, 3995–4005. https://doi.org/10.1029/2018GC007554.

Moore, M.T., Vinson, D.S., Whyte, C.J., Eymold, W.K., Walsh, T.B., Darrah, T.H., Lawson, M., Formolo, M.J., Eiler, J.M., 2018. Differentiating between biogenic and thermogenic sources of natural gas in coalbed methane reservoirs from the Illinois Basin using noble gas and hydrocarbon geochemistry. In: Lawson, M., Formolo, M.J., Eiler, J.M. (Eds.), From Source to Seep: Geochemical Applications in Hydrocarbon Systems. Geological Society of London 468. https://doi.org/10.1144/SP468.8.

Nguyen, T.T.T., Nguyen, L.A.T., Perdomo, G.E.M., 2017. Methodology of Compartmentalization Analysis for Modelling - Mereenie Field, Northern Territory. SPE/IATMI Asia Pacific Oil & Gas Conference and Exhibition. https://doi.org/10.2118/186433-MS.

Oxburgh, E.R., O'Nions, R.K., Hill, R.I., 1986. Helium isotopes in sedimentary basins. Nature 324, 632–635. https://doi.org/10.1038/324632a0.

Ozima, M., Podosek, F.A., 2002. Noble Gas Geochemistry, 2nd edition. Cambridge University Press, New York.

Pinti, D.L., Marty, B., 1995. Noble gases in crude oils from the Paris Basin, France: implications for the origin of fluids and constraints on oil-water-gas interactions. Geochim. Cosmochim. Acta 59, 3389–3404. https://doi.org/10.1016/0016-7037(95)00213-J.

Porcelli, D., Ballentine, C.J., Wieler, R., 2002. An overview of noble gas geochemistry and cosmochemistry. In: Porcelli, D., Ballentine, C.J., Wieler, R. (Eds.), Reviews in Mineralogy and Geochemistry 47, pp. 1–19. https://doi.org/10.2138/rmg.2002.47.1.

Prinzhofer, A., Dos Santos Neto, E.V., Battani, A., 2010. Coupled use of carbon isotopes and noble gas isotopes in the Potiguar basin (Brazil): Fluids migration and mantle influence. Mar. Pet. Geol. 27, 1273–1284. https://doi.org/10.1016/j.marpetgeo.2010.03.004.

Scanlin, M.A., Engelder, T., 2003. The basement versus the no-basement hypotheses for folding within the Appalachian plateau detachment sheet. Am. J. Sci. 303, 519–563. https://doi.org/10.2475/ajs.303.6.519.

Schlegel, M.E., Zhou, Z., McIntosh, J.C., Ballentine, C.J., Person, M.A., 2011. Constraining the timing of microbial methane generation in an organic-rich shale using noble gases, Illinois Basin, USA. Chem. Geol. 287, 27–40. https://doi.org/10.1016/j.chemgeo.2011.04.019.

Shuster, D.L., Farley, K.A., 2005. Diffusion kinetics of proton-induced ^{21}Ne, ^{3}He, and ^{4}He in quartz. Geochim. Cosmochim. Acta 69, 2349–2359. https://doi.org/10.1016/j.gca.2004.11.002.

Smalley, P.C., Muggeridge, A.H., 2010. Reservoir compartmentalization: Get it before it gets you. In: Jolley, S.J., Fisher, Q.J., Ainsworth, R.B., Vrolijk, P.J., Delisle, S. (Eds.), Reservoir Compartmentalization. Geological Society of London, pp. 25–41. https://doi.org/10.1144/sp347.3.

Torgersen, T., 1980. Controls on pore-fluid concentration of 4He and 222Rn and the calculation of ^{4}He/^{222}Rn ages. J. Geochem. Explor. 13, 57–75. https://doi.org/10.1016/j.petrol.2011.07.014.

Wang, Y.J., Fan, W.M., Zhang, G.W., Zhang, Y.H., 2013. Phanerozoic tectonics of the South China Block: key observations and controversies. Gondwana Res. 23, 1273–1305. https://doi.org/10.1016/j.gr.2012.02.019.

Weiss, R.F., 1971a. The effect of salinity on the solubility of argon in seawater. Deep-Sea Res. Oceanogr. Abstr. 18, 225–230. https://doi.org/10.1016/0011-7471(71)90111-2.

Weiss, R.F., 1971b. Solubility of helium and neon in water and seawater. J. Chem. Eng. Data 16, 235–241. https://doi.org/10.1021/je60049a019.

Wen, T., Castro, M.C., Ellis, B.R., Hall, C.M., Lohmann, K.C., 2015. Assessing compositional variability and migration of natural gas in the Antrim Shale in the Michigan Basin using noble gas geochemistry. Chem. Geol. 417, 356–370. https://doi.org/10.1016/j.chemgeo.2015.10.029.

Wen, T., Castro, M.C., Nicot, J.-P., Hall, C.M., Larson, T., Mickler, P., Darvari, R., 2016. Methane sources and Migration Mechanisms in Shallow Groundwaters in Parker and Hood Counties, Texas—a Heavy Noble Gas Analysis. Environ. Sci. Technol. 50, 12012–12021. https://doi.org/10.1021/acs.est.6b01494.

Wen, T., Castro, M.C., Nicot, J.-P., Hall, C.M., Pinti, D.L., Mickler, P., Darvari, R., Larson, T., 2017. Characterizing the noble gas isotopic composition of the Barnett shale and Strawn group and constraining the source of stray gas in the trinity aquifer, North-Central Texas. Environ. Sci. Technol. 51, 6533–6541. https://doi.org/10.1021/acs.est.6b06447.

Wen, Tao, Pinti, Daniele L., Castro, M. Clara, López-Hernández, Aída, Hall, Chris M., Shouakar-Stash, Orfan, Sandoval-Medina, Fernando, 2018. A noble gas and ^{87}Sr/^{86}Sr study in fluids of the los azufres geothermal field, Mexico – Assessing impact of exploitation and constraining heat sources. Chem. Geol. 483, 426–441. https://doi.org/10.1016/j.chemgeo.2018.03.010.

Yan, D.P., Zhou, M.F., Song, H.L., Wang, X.W., Malpas, J., 2003. Origin and tectonic significance of a Mesozoic multi-layer over-thrust system within the Yangtze Block (South China). Tectonophysics 361, 239–254. https://doi.org/10.1016/s0040-1951(02)00646-7.

Zartman, R.E., Wasserburg, G.J., Reynolds, J.H., 1961. Helium, argon, and carbon in some natural gases. J. Geophys. Res. 66, 277–306. https://doi.org/10.1029/JZ066i001p00277.

Zhou, Z., Ballentine, C.J., 2006. ^{4}He dating of groundwater associated with hydrocarbon reservoirs. Chem. Geol. 226, 309–327. https://doi.org/10.1016/j.chemgeo.2005.09.030.

Zhou, Z., Ballentine, C.J., Schoell, M., Stevens, S.H., 2012. Identifying and quantifying natural CO_2 sequestration processes over geological timescales: the Jackson Dome CO_2 Deposit, USA. Geochim. Cosmochim. Acta 86, 257–275. https://doi.org/10.1016/j.gca.2012.02.028.